PRELIMINARY INVESTIGATION OF RADIATION PHENOMENA IN HIGH PRESSURE AIR AND ARGON CASCADE ARCS

A THESIS

Presented to

The Faculty of the Division of Graduate Studies and Research

by

Daniel P. Dodson

In Partial Fulfillment

of the Requirements for the Degree

Master of Science in Mechanical Engineering

Georgia Institute of Technology

December, 1977

PRELIMINARY INVESTIGATION OF RADIATION PHENOMENA IN HIGH PRESSURE AIR AND ARGON CASCADE ARCS

Approved:

Dr. A. V. Larson

Dr. W. Z. Black

Dr. P. V. Desai

Date approved by Chairman: 12/5/77

ACKNOWLEDGMENTS

I am deeply grateful to my parents for their guidance and support throughout my academic pursuits.

I will always be indebted to Dr. A. V. Larson and R. T. Murray . I wish to thank Dr. Larson, who awakened my quest for knowledge, for his unending time and guidance in my academic pursuits. To Bob Murray, who kindled my enthusiasm for experimental research, I wish to express my gratitude for his support, patience, and guidance in the development of my laboratory expertise.

I wish to thank Drs. W. Z. Black, P. V. Desai, and R. B. Evans for their time and consultation in my education.

To my fellow students, Chris Christy and Thad Salmon, I wish to thank you for the support and friendship I received during this program.

I would also like to thank the Department of the Air Force and the Arnold Engineering Development Center which, under Contract No. F40600-77-C-0007, managed by Dr. M.L. Laster, Technical Monitor, and Mrs. Ernestine Badman, Contract Officer, has made this work possible.

TABLE OF CONTENTS

LIST OF TABLES

LIST OF ILLUSTRATIONS

NOMENCLATURE

A_{ki}	Einstein transition probability for spontaneous emission prob/sec-atom
c_o	speed of light 2.99×10^8 m/s
dI_λ	differential intensity change in length dx watt/m^3-sr
dx	differential length m
E_i	lower electronic energy level joule
E_{j_k}	energy level of upper atomic state joule
E_k	upper electronic energy level joule
E_{k_1}, E_{k_2}	upper electronic energy level of specific line joule
g_k	statistical weight of the k^{th} electron state
h	Plank's constant 6.624×10^{-34} joule-sec
$I_{a_\lambda}(y)$	arc intensity at exit of plasma column watt/m^3-sr
$I_\ell(P,T,x_j)$	line intensity watt/m^2-sr
$I_{\lambda_{BB}}$	blackbody intensity watt/m^3-sr
$I_\lambda(x)$	spectral intensity at x W/m^3-sr
$I_\lambda(y)$	measured intensity at y watt/m^3-sr
$I^a_\lambda(y)$	measured arc intensity through apparatus (source off) watt/m^3-sr
$I^s_\lambda(y)$	measured source intensity through apparatus watt/m^3-sr
$I^s_{\lambda_o}(y)$	measured source intensity through evacuated apparatus watt/m^3-sr
k	Boltzmann constant 1.3804×10^{-23} joule/°K
$k_\lambda(x)$	spectral absorption coefficient m^{-1}

$k_1(x)$	spectral absorption coefficient in arc m^{-1}
k_2, k_3	spectral absorption coefficients in optical path m^{-1}
L_1, L_2, L_3	optical path absorption lengths m
m_e	electron mass 9.1086×10^{-31} kg
n_e	number density of electrons m^{-3}
n_z	number density of ions of charge z m^{-3}
n_{z+1}	number density of ions of charge z+1 m^{-3}
$N_{j_k}(P,T)$	number density of atoms of type j in energy level k m^{-3}
N_j	number density of atoms of type j m^{-3}
P	pressure atmospheres
R	universal gas constant
R_e	line intensity ratio
T	temperature °K
$U_j(T)$	partition function of species j
U_z	partition function of the z ions
U_{z+1}	partition function of the z+1 ions
ν_{ki}	frequency of line emitted sec^{-1}
x	position along the optical path m
X_j	molar fraction of species j
y	off-axis position of the optical path m
$\varepsilon_\ell(P,T,x_j)$	line emission coefficient as a function of thermodynamic state and wavelength watt/m^3-sr
$\varepsilon_{\ell j}$	line emission intensity of species j W/m^3-sr
ε_λ	spectral emission coefficient W/m^4-sr
λ_c	continuum wavelength m

λ_{ki}	wavelength of line emitted	
λ_{o_ℓ}	line center wavelength	m
$d\lambda$	differential wavelength interval	m
$\Delta\lambda$	line wavelength interval	m
Φ	ionization potential	joule
$\Delta\Phi$	lowering of ionization potential	joule

SUMMARY

Preliminary spectroscopic information on air and argon plasmas at pressures from 1 to 100 atmospheres at a temperature of approximately 10,000°K was obtained in the wavelength region from 300-900 nm. The plasma discharges were contained in a steady-state wall-vortex stabilized cascade arc of diameter 3 mm operating at currents from 10 to 15 amperes.

The emission of an argon arc was measured by side-on observation of a cylindrical plasma column at pressures of 1, 30, and 100 atmospheres. Air plasma emission was measured at pressures of 1, 10, and 30 atmospheres. A secondary light source was used in a chopped light technique to measure absorption along the optical path of the arc radiation. Argon arcs were found to exhibit slight spectral absorption at a wavelength of 546.4 nm. Air arcs were found to exhibit strong spectral absorption at a wavelength of 546.4 nm due to the formation of NO_2 and other byproducts in the outer boundary of the arc. In addition, strong refractive effects were found to exist at the arc channel wall due to the presence of strong thermal gradients in the boundary layer.

CHAPTER I

INTRODUCTION

The engineering design of high temperature and pressure plasma phenomena requires the basic knowledge of the transport and thermodynamic properties of the system. The design of spacecraft for reentry is currently being simulated at the Arnold Engineering Development Center with plasma air streams created by electric arc heaters [1]. The design of high power high enthalpy arc heaters to optimize the balance of electrical energy conversion to thermal and radiant energy at pressures of 250 atmospheres and temperatures of 10,000°K requires an understanding of the electrical and the thermal conductivity, radiant emission and absorption, viscosity, and thermodynamic state composition of the carrier gas.

These properties may be obtained by experimental measurement or by theoretical predictions via semi-empirical equations whose constants are adjusted to match available experimental data. The effects of dissociation and ionization and the change in dominant particle collision interactions at higher pressures make the extrapolation of low pressure-low temperature semi-empirical equations to higher pressures and temperatures subject to error.

The wall stabilized, steady state, direct current arc

is currently being used at Georgia Tech to experimentally measure properties at high pressures. The side-on observation of the cylindrically symmetric arc allows the volume emission coefficient to be determined from the lateral intensity profile via the Abel Inversion [2]. The temperature may subsequently be found from theoretical predictions of the emission as a function of the thermodynamic state of the radiating species. Thereafter, the measured current, electric field strength, total volume emission and temperature profile allow the deduction of the electrical and thermal conductivity, and the radiation source strength. Air and argon arcs are currently being created at pressures of up to 140 atmospheres in current ranges of 15-25 amperes in arc channels of 2-5 mm diameter. Experimental data on air at pressures of 1, 6 and 30 atmospheres by Larson [3] and on argon up to 200 atmospheres by Devoto [4] and Wynn [5] have been published.

The prediction of the thermodynamic state from theoretical statistical physics has been done by many authors. However, the presence of non-ideal effects [6,7], diffusion effects from strong thermal gradients [8,9], and possibly neglected chemical reactions [10,11] in plasma devices may lead to discrepancies between the theoretically predicted and experimentally measured behavior. In addition, the spectral characteristics are continually changing with pressure. Spectral absorption [21,22,23], broadening effects [12], and refraction effects [13,14] may necessitate the use or development

of more complicated diagnostic techniques. The diagnostics of line,continuum, and band emission measurement techniques at higher pressures may not be applicable.

The results of an experimental spectroscopic investigation are presented in this paper. The goal of the program was to examine certain optical phenomena to assess their influence on the selection of the methods, such as line emission techniques, which are available for the determination of the thermodynamic state of the plasma. Relative surveys on the spectra of an argon arc at pressures of 1, 30, and 100 atmospheres from 350 nm. to 900 nm. and of an air arc at 1, 10, and 30 atmospheres from 600 nm. to 900 nm. are presented. The absorption and refraction characterstics of the optical path of the cascade arc device are obtained at a pressure of 30 atmospheres and wavelengths from 350 nm. to 600 nm. for air an argon arcs. The design, construction,and operation of the cascade arc with a 3 mm. diameter channel of length 30 mm. operating at a current of 15 to 25 amperes at pressures to 100 atmospheres with a centerline temperature of approximately 10,000°K are given for air and argon arcs.

CHAPTER II

THEORY

The spectral diagnostics of inhomogeneous radiating plasmas surrounded by an absorbing medium require that the measured intensity be corrected for optical losses. The spectral emission and absorption are a function of the thermodynamic state of the plasma, the wavelength of the radiation, and the properties of the optical path. Of major importance is the temperature profile in the arc which can be deduced via the correlation of the corrected measured intensity and theoretical statistical thermodynamics if the self-absorption within the arc is not too great.

The thermodynamic state of the plasma determines the spectral emission and absorption of the atoms, ions, electrons, and molecules which occur in the mixture. The excitation, de-excitation, ionization, and recombination processes are assumed to be collision dominated by electronic interactions. The gas mixture of neutrals and ions is assumed to be in local thermodynamic equilibrium with the electron gas at the equilibrium temperature based on the statistical physics of an ideal gas.

The atoms, ions, electrons, and molecules emit a spectrum of radiation from the infrared to the ultraviolet wavelengths. The emission is composed of line, continuum

and band spectra. The line emission spectra is governed by the bound-bound transitions; the continuum emission is a sum of free-bound and free-free electronic transitions, and the band spectra is composed of molecular bands which are related to the rotational and vibrational transitions of the molecule.

The line, continuum, and band absorption are characteristic of the plasma state [12]. Spectral absorption across a line is proportional to the intensity of the line emission. Continuum absorption is usually very weak in the ultraviolet and visible regions except for electron number densities of approximately 10^{20} cm^{-3}. However, it is stronger in the infrared region with electron number densities of approximately 10^{16} - 10^{17} cm^{-3}. Molecular band absorption does not exist in the plasma arc except at the lower temperature regions which occur in the outer boundary.

The total spectral emission of the plasma is composed of the line, continuum, and band spectra. Temperature determination techniques based on the theoretical and semi-empirical predictions of the emission coefficient from the plasma in a certain thermodynamic state are applicable to the three types of spectra. The suitability of a particular diagnostic method is dependent upon the characteristics of the radiation and the magnitude of the error involved in deducing the temperature. A preliminary survey of the

emission spectra at various temperatures and pressures is necessary to determine the most accurate method available. Knowledge of the general behavior of the spectra as the pressure is increased will allow preliminary low pressure arc diagnostics to be used to select candidate lines for study at higher pressure levels.

The line emission spectra are available from the infrared to the ultraviolet with relatively low error estimates [15]. The wavelength of specific lines is determined by the energy change of the electronic transition:

$$E_k - E_i = h\nu_{ki} = hc_o/\lambda_{ki} \tag{1}$$

where

E_k = upper electronic energy level

E_i = lower electronic energy level

h = Plank's constant

c_o = speed of light

ν_{ki} = frequency of line emitted

λ_{ki} = wavelength of line emitted

The power emitted per unit volume per unit solid angle is known as the line emission coefficient, ε_{ℓ_j}, and is given by

$$\varepsilon_{\ell_j}(P,T,X_j) = \frac{hc_o}{4\pi\lambda_{ki}} A_{ki} N_{j_k}(P,T) \tag{2}$$

where A_{ki} is the spontaneous transition probability, and N_{j_k} is the number of atoms of type j in energy level k per unit volume.

The plasma particles are assumed to have a Maxwellian velocity distribution with temperature T. The number of atoms of type j in energy level k is given by the Boltzman distribution function as

$$N_{j_k} = \frac{N_j g_k}{U_j(T)} \exp(-E_{j_k}/kT) \tag{3}$$

where

N_j = number density of atoms of type j

g_k = statistical weight of upper level

$U_j(T)$ = partition function

E_{j_k} = energy level of upper state k of species j

k = Boltzman's constant

The number density of atoms of type j in a plasma volume element is related to the jth molar fraction in accordance with Dalton's Law.

$$N_j = X_j \frac{P}{RT} \tag{4}$$

where X_j is the molar fraction of the jth species at the temperature T and pressure P of the volume element.

The equilibrium composition of air plasma has been calculated by Predvoditelev [16]. The method of statistical

physics was used in which air was considered to be 78.08% N_2, 20.95% O_2, and 0.97% Ar at normal conditions. The dissociation of N_2 and O_2, formation of NO, and single ionization of N_2, O_2, NO, N, O, and Ar were solved in a system of 13 simultaneous non-linear equations for various temperatures and pressures. Hence the molar fraction is predicted as a function of temperature and pressure based on ideal gas assumptions neglecting interactions between gas particles.

In a study by Devoto [4], the equilibrium composition of an argon plasma was computed by an extension of the Boltzman distribution to consecutive ionization stages of the argon atom resulting in the Saha equation [12].

$$\frac{n_e n_{z+1}}{n_z} = \frac{2U_{z+1}(T)}{U_z(T)} \frac{(2\pi m_e kT)^{3/2}}{h^3} \exp\left(\frac{\phi - \Delta\phi}{kT}\right) \qquad (5)$$

where

n_e = number density of electrons

n_{z+1} = number density of ions of charge z+1

n_z = number density of ions of charge z

$U_{z+1}(T)$ = partition function of the z+1 ion

$U_z(T)$ = partition function of the z ion

m_e = electron rest mass

ϕ = ionization potential for z+1 ionization

$\Delta\phi$ = lowering of the ionization potential.

Values of $U_{z+1}(T)$, $U_z(T)$, ϕ, and $\Delta\phi$ were obtained from

Drawin and Felenbok [17]. Assuming plasma charge neutrality, the ideal gas equation of state, and local thermodynamic equilibrium, the molar fractions in an argon plasma were computed at various temperatures and pressures.

Using equations 2, 3, and 4, the line emission coefficient of the plasma as a function of the thermodynamic state and wavelength is given by

$$\varepsilon_{\ell_j} = \frac{hc\, A_{ki}\, g_k}{4\pi\, \lambda_{ki} R} \frac{X_j P}{T U_j} \exp(-E_{j_k}/kT) \qquad (6)$$

The value of the transition probability and statistical weight are obtained from the National Bureau of Standards [18].

The corrected intensities of emission from lines can be used to deduce the temperature of the plasma in several ways [12]. In an optically thin plasma (no self-absorption), one standard procedure is as follows. For a particular line, the intensity of the plasma radiation is determined over a wavelength band which includes all of the line radiation. The spatially measured radiation intensity via side-on viewing of the arc is used to deduce the volume emission coefficient (which is a function of the off-axis position (y) by use of the Abel inversion technique. The absolute line intensity is obtained by subtracting the intensity at a neighboring continuum wavelength λ_c from the total intensity measured at the line wavelength $\lambda_{o\ell}$ as shown in Figure 1a,b,c. The intensity profiles can be calibrated with a standard

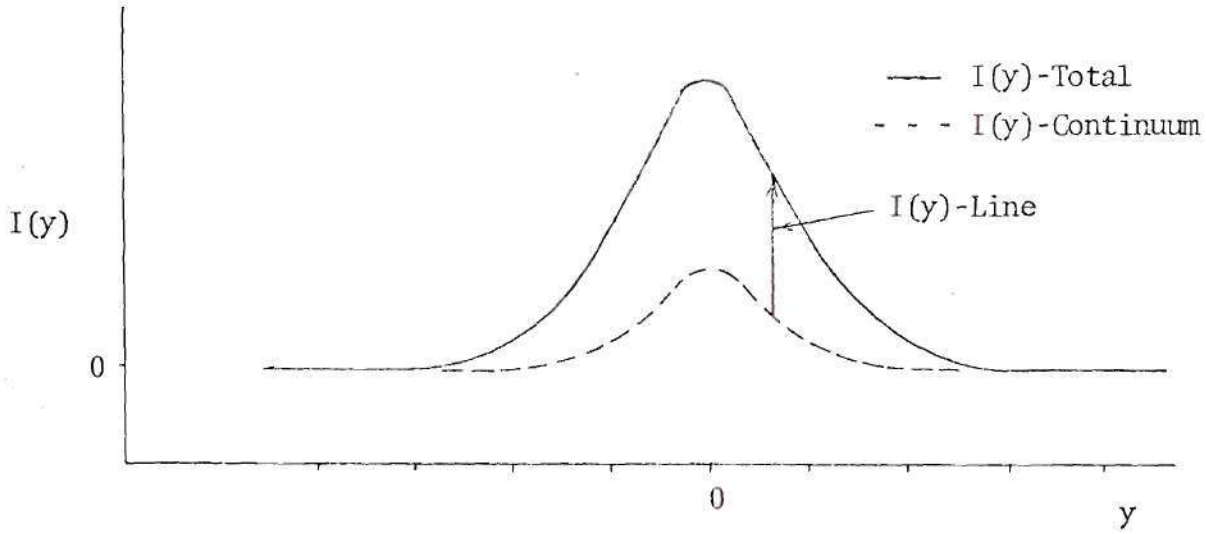

Figure 1a. Spatial Scan of Total Radiation at λ_{o_ℓ} of Wavelength Interval $\Delta\lambda$

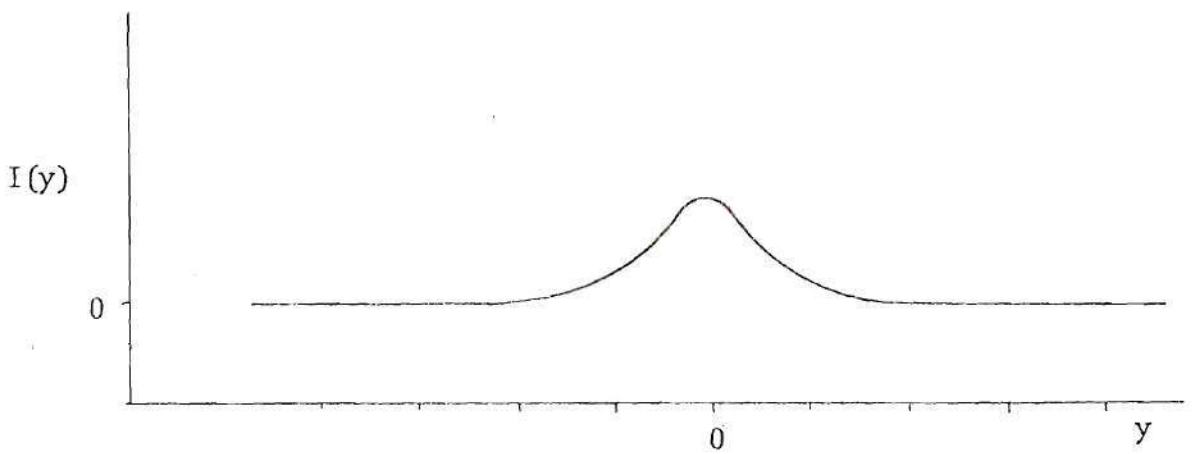

Figure 1b. Spatial Scan of Continuum Radiation at λ_c of Wavelength Interval $\Delta\lambda$

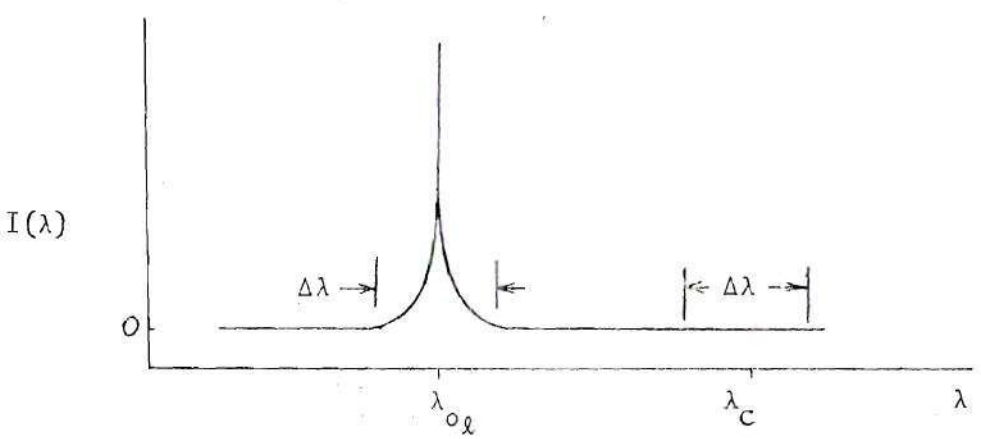

Figure 1c. Spectral Scan at Arc Center , y=0

source to convert the amplitude on the strip chart to intensity in watts/sr-m^2.

The absolute line intensity can be used directly or in a ratio technique with the intensities of other lines from the radiating mixture. The relative error in deducing the temperature by these techniques is governed by the knowledge of the theoretical relationships and the accuracy of the experimental measurements. The accuracies of the measured emission coefficients and transition probabilities are major parameters in the accuracy of the temperature deduction. Equation (6) may be put in the form of

$$\varepsilon_{\ell_j} = K \frac{A_{ki}}{T} \exp(-E_{j_k}/kT) \tag{7}$$

where K is a constant based on the remaining parameters which are assumed known. Hence

$$\varepsilon_{\ell_j} = \varepsilon_{\ell_j}(A_{ki}, T) \tag{8}$$

and the error in ε_{ℓ_j} is related to the errors in A_{ki} and T by

$$d\varepsilon_{\ell_j} = \frac{\partial \varepsilon_{\ell_j}}{\partial A_{ki}} dA_{ki} + \frac{\partial \varepsilon_{\ell_j}}{\partial T} dT. \tag{9}$$

Using (7) and (9), the relative error of the deduced temperature is given by

$$\frac{dT}{T} = \left[\frac{d\varepsilon_{\ell_j}}{\varepsilon_{\ell_j}} + \frac{dA_{ki}}{A_{ki}} \right] \frac{kT}{E_{j_k}} \quad . \tag{10}$$

The intensity ratio of two lines from the same species is given by

$$R_e = \frac{\varepsilon_{\ell_1}}{\varepsilon_{\ell_2}} = \frac{\nu_1 A_1 g_1}{\nu_2 A_2 g_2} \exp\left[- \frac{E_{k_1} - E_{k_2}}{kT} \right] \tag{11}$$

and the relative error is given by

$$\frac{dT}{T} = \left[\frac{d(\varepsilon_{\ell_1}/\varepsilon_{\ell_2})}{\varepsilon_{\ell_1}/\varepsilon_{\ell_2}} + \frac{d(A_1/A_2)}{A_1/A_2} \right] \frac{kT}{E_{k_1} - E_{k_2}} \tag{12}$$

The total line emission (equation (6)) undergoes broadening mechanisms which distribute the energy of emission over a finite range of wavelengths called the line width, $\Delta\lambda$.

Hence, the accuracy of measurement of the line intensities within the arc is dependent upon the knowledge of the spectral absorption along the optical path. Referring to Figure 2, the total absorption is due to the arc and the surrounding medium via the line, continuum, and band absorption at any given wavelength. Since the arc radiation intensity is a priori unknown, a secondary calibrated light source can be used to measure the spectral absorption along

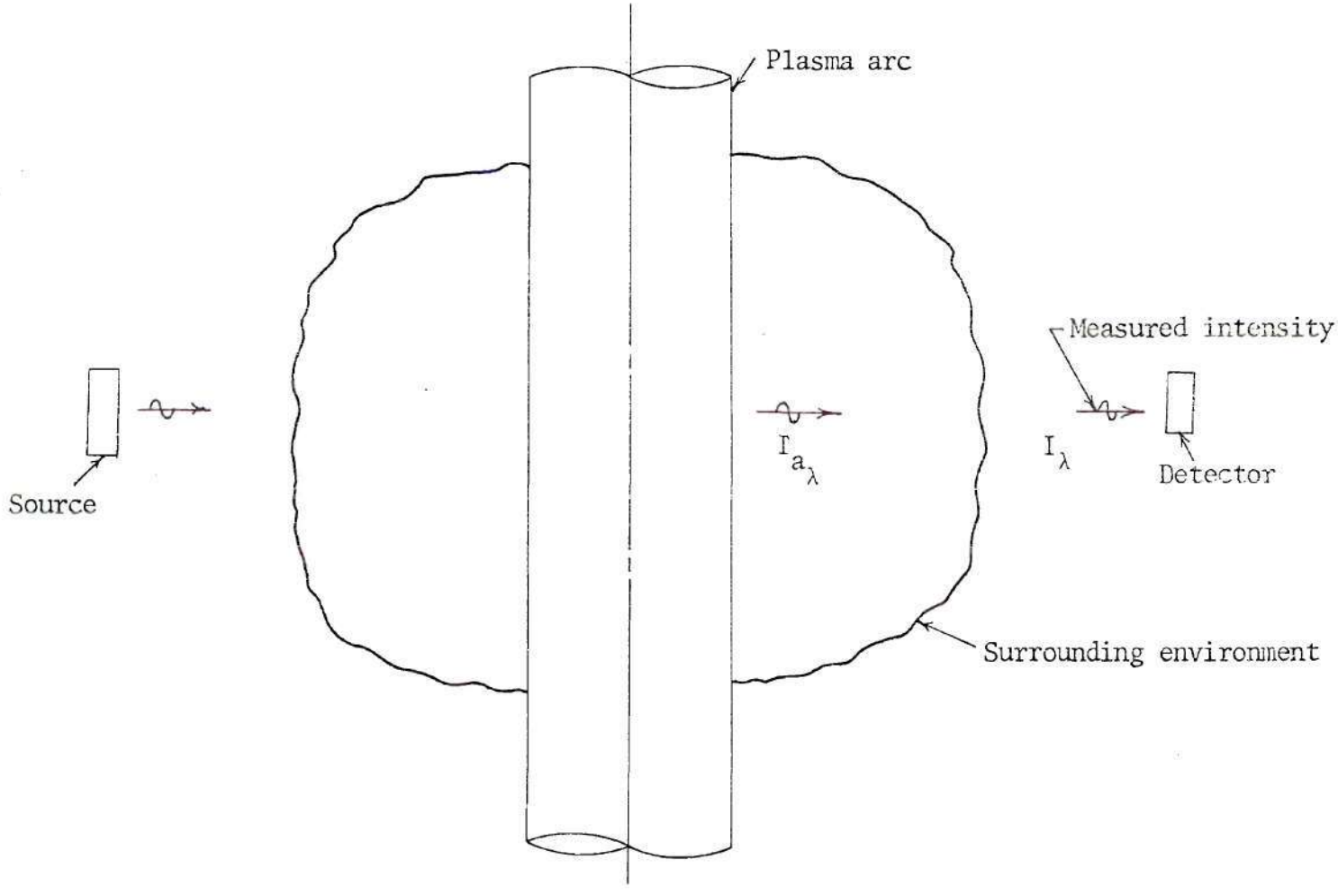

Figure 2. Optical Path

the total optical path from which estimates of the absorption effect on the arc radiation can be deduced.

The plasma column shown in Figure 3a is assumed cylindrically symmetric in which the x-coordinate lies along the line-of-sight (the optical path) and the y-coordinate determines the off axis position of the line of sight. The measured spectral intensity at any y is determined by the distribution of the absorption and emission coefficients along the line of sight.

The change of the intensity at a wavelength λ, as it passes through an absorbing and emitting layer as shown in Figure 3b is given by

$$dI_\lambda = \{\varepsilon_\lambda(x) - k_\lambda(x) I_\lambda(x)\}dx \qquad (13)$$

where

dI_λ = differential change in intensity
$\varepsilon_\lambda(x)$ = spectral emission coefficient
$k_\lambda(x)$ = spectral absorption coefficient
$I_\lambda(x)$ = entering radiation intensity
dx = differential length

Hence, the measured intensity at y at wavelength λ is given by

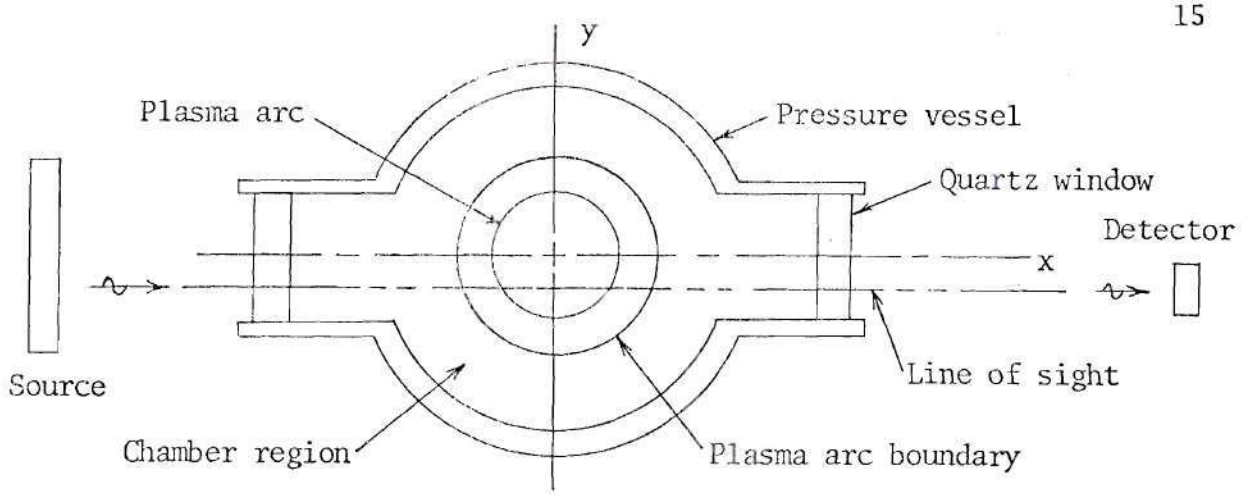

Figure 3a. Plasma Arc Geometry

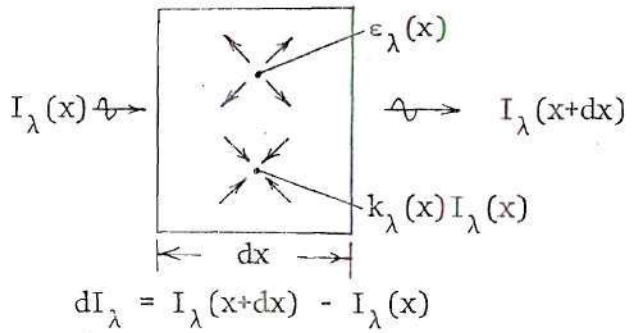

Figure 3b. Net Radiation from Differential Volume

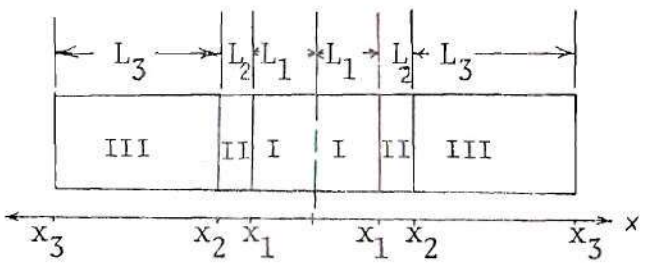

Figure 3c. Optical Path in Chamber

$$I_\lambda(y) = \int_{-x_3}^{x_3} \varepsilon_\lambda(x) \exp\{-\int_{-x'}^{x_3} k_x(x')dx'\}dx +$$

$$I^s_{\lambda_o}(y) \exp\{-\int_{-x_3}^{x_3} k_\lambda(x)dx\} \qquad (14)$$

It is convenient in this work to evaluate $I_\lambda(y)$ by assuming the existence of three absorbing and emitting regions as shown in Figure 3c. The intensity measured by the spectrometer $I_\lambda(y)$ can be expressed as

$$I_\lambda(y) = I_{a_\lambda}(y) \exp\{-k_2L_2-k_3L_3\} +$$

$$I^s_{\lambda_o}(y)\exp\{-2(k_1L_1+k_2L_2+k_3L_3)\} \qquad (15)$$

where homogeneous absorption regions II and III with absorption coefficients k_2 and k_3 lie in the immediate vicinity of the arc and the remainder of the optical path within the vessel respectively, and the lengths of regions I, II, and III are given by L_1, L_2, and L_3. The arc intensity, $I_{a_\lambda}(y)$, and the arc optical depth, $2k_1L_1$ are given by

$$I_{a_\lambda}(y) = \int_{-x_1}^{x_1} \varepsilon_\lambda(x)\exp\{-\int_{-x'}^{x} k_1(x')dx'\}dx \qquad (16)$$

$$2k_1L_1 = \int_{-x_1}^{x_1} k_1(x)dx \qquad (17)$$

It is of course $I_{a_\lambda}(y)$ which is needed in order to deduce the temperature profile within the arc.

The use of the secondary light source allows the total path absorption to be measured via a subtraction technique. Equation (15) can be used with two intensity measurements in which the source is off and on. They may be subtracted to give

$$I^s_\lambda(y) = I^s_{\lambda_o}(y)\, \exp\{-2(k_1L_1+k_2L_2+k_3L_3)\} \qquad (18)$$

where $I^s_\lambda(y)$ is the measured intensity of the source.

Similarly, if the source radiation is chopped, a lock-in amplifier can be used to measure the absorption effect by rejecting the steady arc radiation. The results of this method may be compared to the subtraction technique to allow internal checks on experimental consistency. The magnitude of the absorption effect on the arc radiation in the environment may be estimated by assuming cylindrical symmetry and using equation (18) to get

$$\frac{I^a_\lambda(y)}{I_{a_\lambda}(y)} \sim \sqrt{\frac{I_\lambda(y)}{I_{\lambda_o}(y)}} = \exp(-k_1L_1-k_2L_2-k_3L_3) \qquad (19)$$

where the arc radiation path is approximately 1/2 the total path. The approximation becomes an equality as $k_1 L_1$ goes to zero.

An iterative procedure may then be used to deduce $\varepsilon(x,y)$ and hence $T(r)$. First an optically thin arc is assumed, i.e. $k_1 = 0$. Then equations (16) and (19) are solved for $\varepsilon_\lambda(x,y)$ by means of the Abel Inversion [2]. Since

$$\varepsilon_\ell = \int_{\Delta\ell} \varepsilon_{\ell_\lambda} \, d_\lambda \tag{20}$$

Equation (6) may be used for the first estimate of $T_i(x,y)$. Then Kirchoff's Law

$$k_\lambda = \frac{\varepsilon_\lambda}{I_{\lambda_{BB}}} \tag{21}$$

is used to obtain the first estimate of the spectral absorption coefficient within the arc.

$I_{\lambda_{BB}}(T)$ is the blackbody radiation intensity (Plank intensity function) at the temperature of the plasma.

$$I_{\lambda_{BB}}(T) = \frac{2hc_1}{\lambda^5 \left[\exp\left(\frac{hc_2}{\lambda kT}\right) - 1 \right]} \tag{22}$$

If k_λ is not too large, it is inserted into (17) and

(19) and the calculation repeated with a better estimate for k_1. The iteration is continued until a self-consistent solution appears. The method will fail if the arc self reabsorption is too great for then I_{a_λ} represents the conditions only at the surface of the arc.

CHAPTER III

APPARATUS

The plasma arc is confined in a 3 mm diameter cylindrical cascade channel which is formed by a vertical stack of water cooled pure copper plates as shown in Figure 4a. A conical thoriated tungsten cathode and hollow tungsten anode are located at the ends of the channel to provide arc fixation points. The plates are electrically insulated by lexan while gas and water systems are sealed with high temperature silicone rubber gaskets. A nonconducting water channel is maintained by the circulation of deionized water from the upper and lower manifolds through diagonally opposed injection channels formed by the cascade stack as shown in Figure 4b. The water cooling channels engraved in the lower sheet of the two piece silver bonded plates allow a high cooling rate to be obtained within 1 mm of the arc channel.

Specific gases are injected into the arc channel at the cathode, anode, and test sections. The argon gas injection at the cathode and anode allow a pure argon arc to be maintained independent of the chamber environment. Reactive test gases are introduced in the central portion of the arc channel by vortex injection through special silicon rubber gaskets located between the cascade plates. The electrode

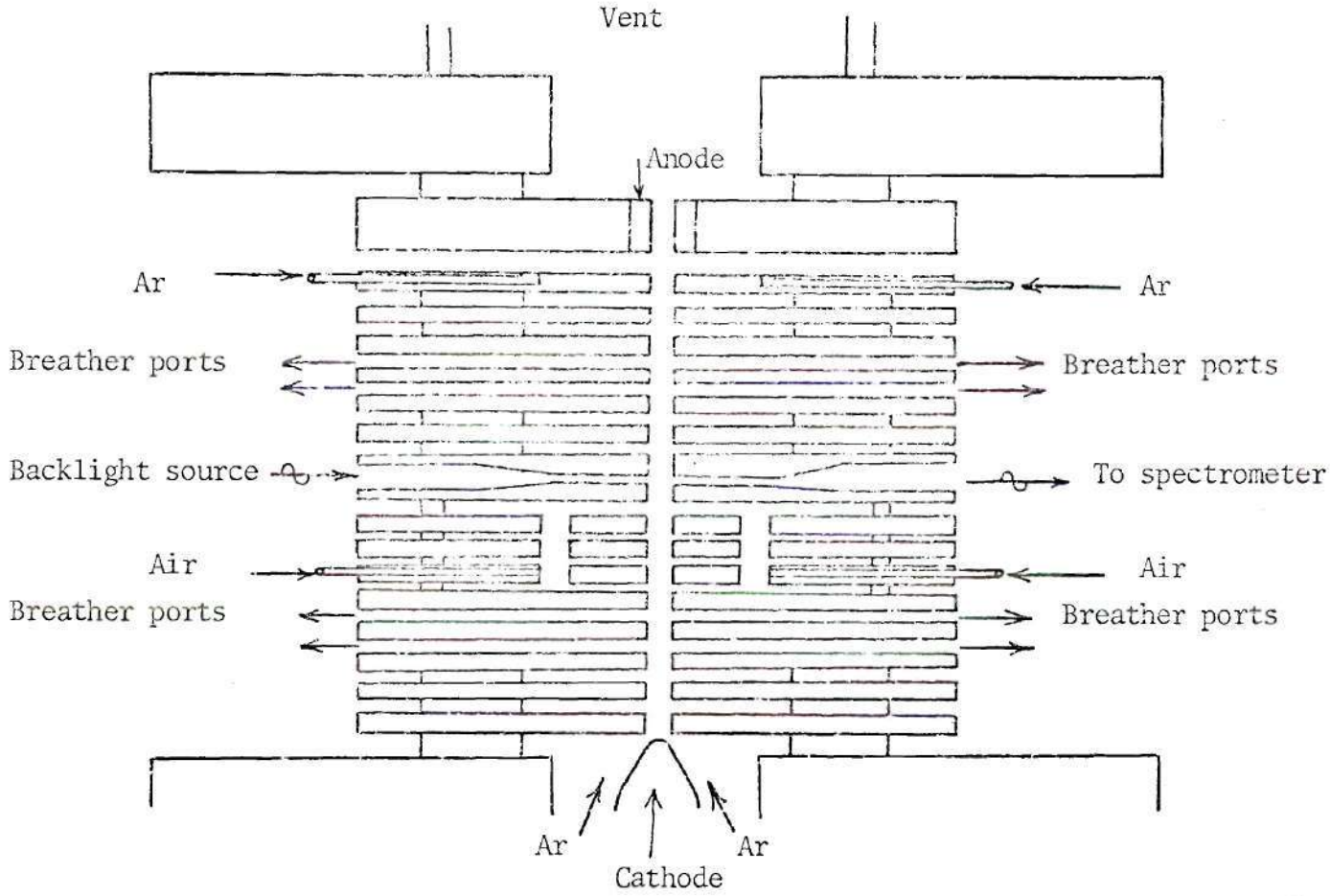

Figure 4 a. Cascade Arc Device

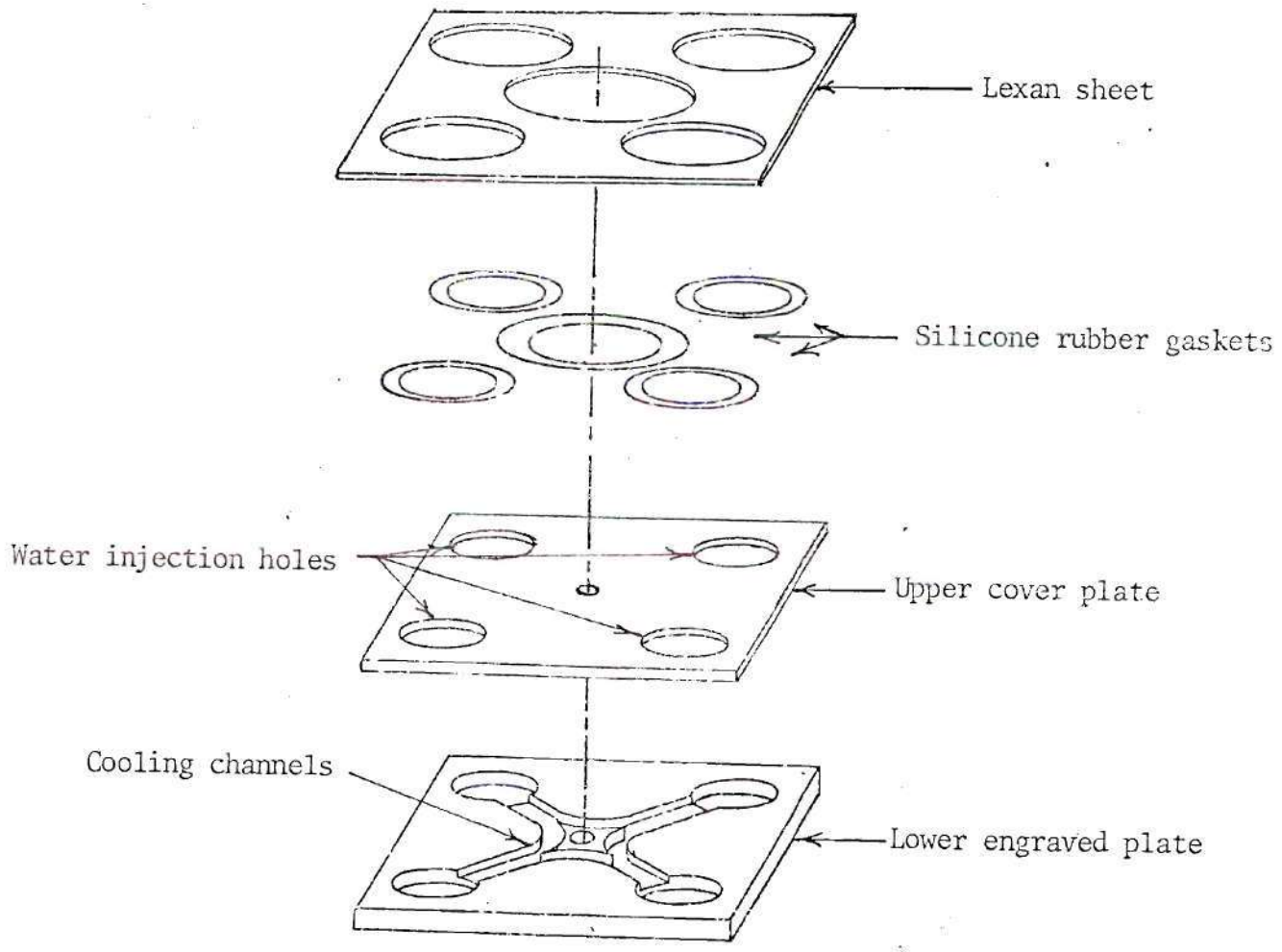

Figure 4b. Exploded Cascade Plate and Gaskets

gas flows are maintained in opposing vortex directions to prevent contamination of the test gases via entrainment of the gas mixtures within the channel. The partially stagnated interface gas mixtures formed by the opposing vortex interactions are vented into the chamber area by the breather ports located between the electrodes and test section. The hot sheath gases at the anode are allowed to flow into the chamber vent region as cool argon gas is injected into the channel to aid in transpiration cooling of the core gases. The overall arc channel gas flow characteristics are controlled by the sealed vent area above the cascade manifold at the anode.

A semi-automatic gas control system maintains the selected flow and pressure conditions of the chamber and cascade injection system as shown in Figure 5. The working pressure of the chamber is maintained by a gas bottle manifold capable of continuous pressures up to 200 atmospheres. Specific gas systems are individually controlled to provide a constant mass flow rate and injection pressure differential at the cathode, anode, and test sections. The gas system is automatically controlled once stable arc conditions are obtained for diagnostics.

A high pressure stainless steel chamber is used to maintain the working pressure of the cascade arc. Electrical, gas, and water connections to the cascade assembly are accomplished by high pressure feed-through fittings located in the end plugs of the chamber. A pressure accumulator

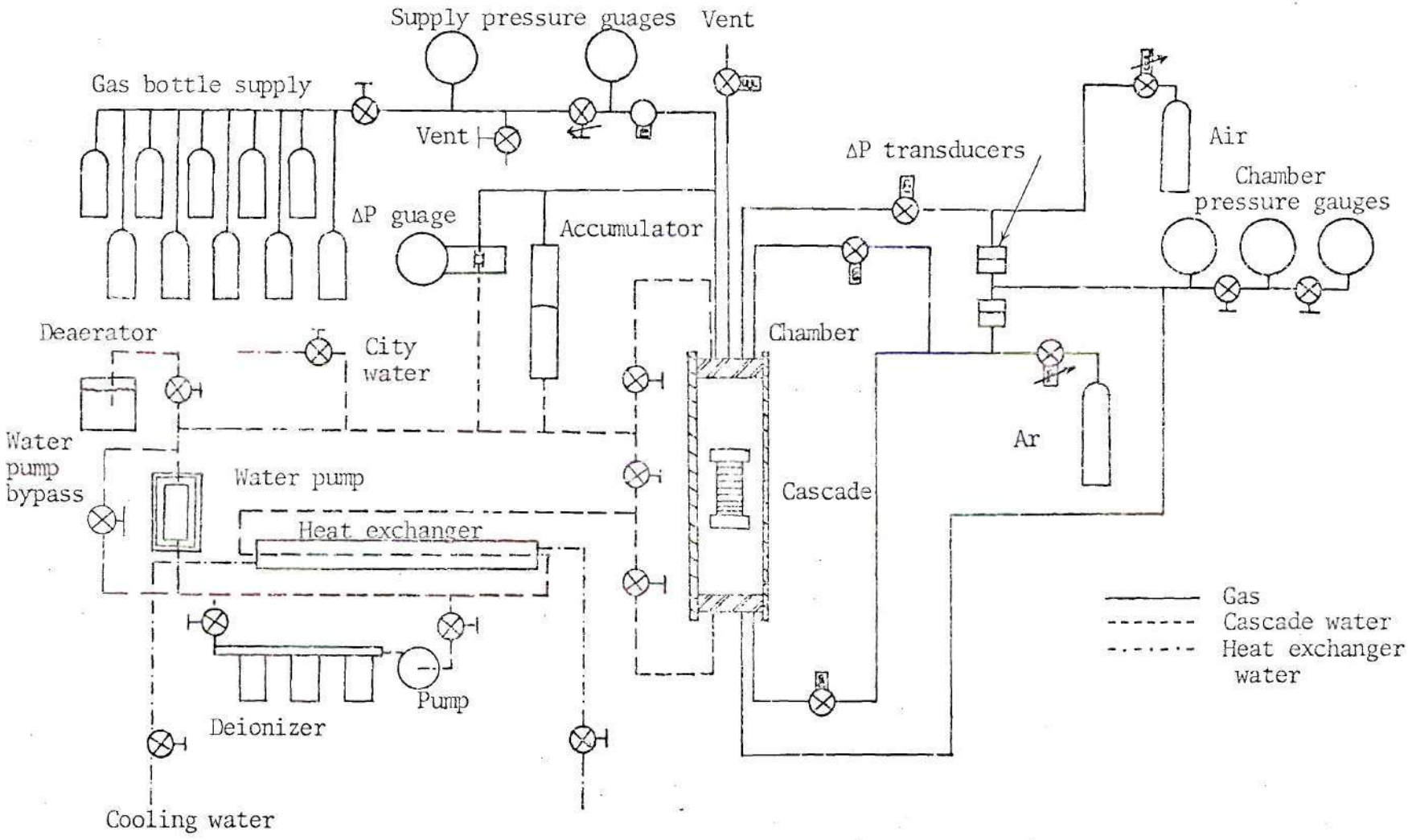

Figure 5. Gas and Water Systems

with a steel bladder maintains pressure equilibrium between the gas and water systems without gas absorption. A submergible water pump and single pass heat exchanger provide cooling at a constant flow rate to the cascade at the chamber pressure.

The window area for observation of the arc in the test section is formed by two customized cascade plates. The plate gap is maintained at a minimum spacing to prevent schlieren effects while the expansion cavities formed by the window plates are platinum blacked to prevent reflections in the optical path.

The optical path of the window area is backlighted with chopped radiation from a 100W Oriel mercury lamp. The side-on image of the arc column and lamp are reflected off a front surface mirror and focused through a limited aperture, sapphire lens onto the entrance slit of the spectrometer as shown in Figure 6.

A helium neon 632.8 nm laser beam is used for the alignment of the spectrometer and window area optical axes and for the placement of the lens, mirror, and mercury lamp. A calibration rod placed in the arc channel allows focusing of the arc axis onto the spectrometer. Adjustable optical quality beamshifters are located between the chamber window and the mercury lamp and in front of the spectrometer for optimum vertical alignment of the optical path.

The composite radiation signal output from the EMI 9658R-S20 photomultiplier tube is measured by a Keithley

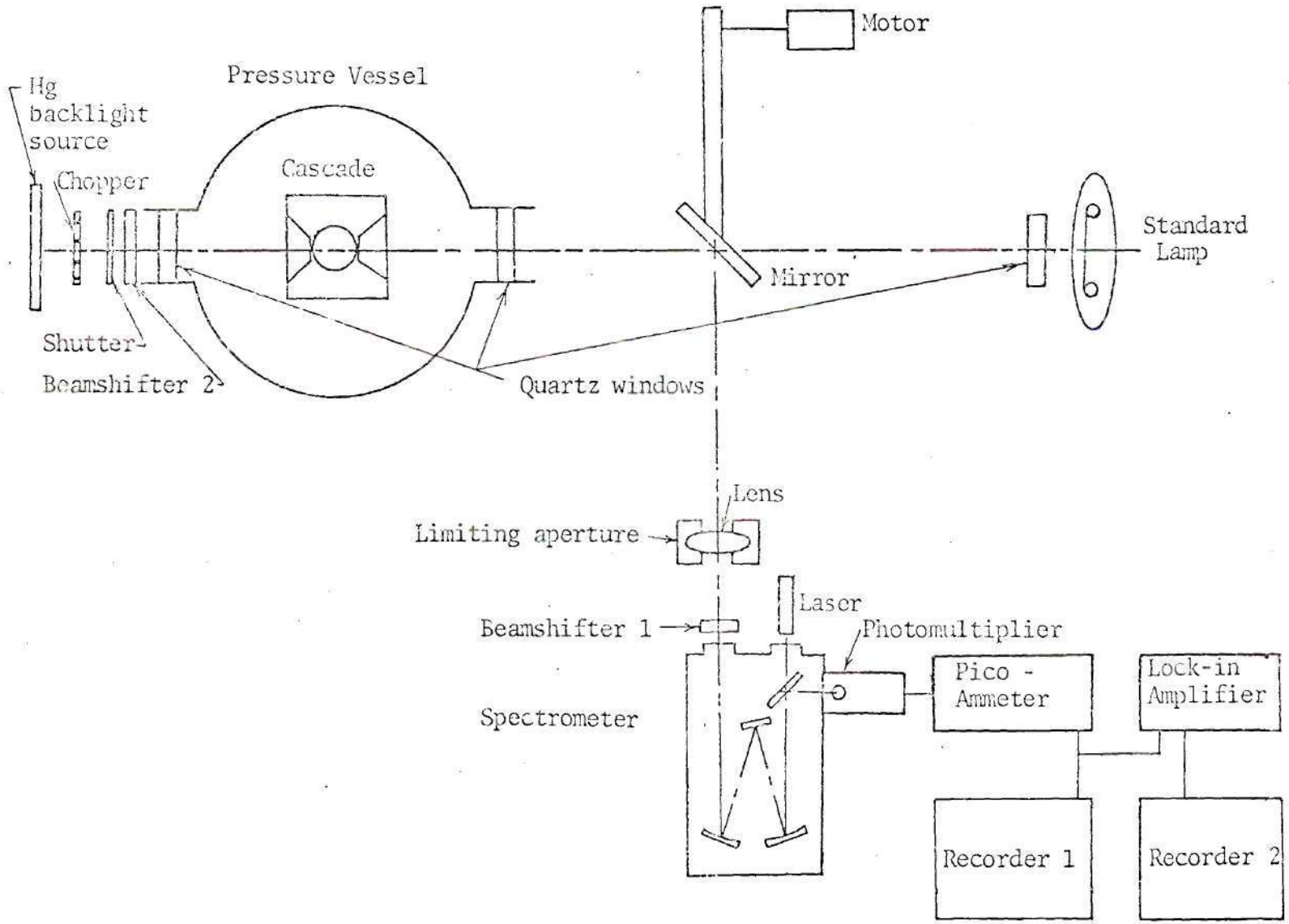

Figure 6. Schematic of Experimental Apparatus

Model 416 picoammeter. A Princeton Applied Research JB-5 lock-in amplifier measures the chopped radiation signal contained on the picoammeter output. A Clevite Brush Mark 250 and H.P. Model 7100 BM recorder simultaneously plot the total and chopped outputs from the picoammeter and lock-in amplifier, respectively. The backlighting of the optical path is selectively controlled by a shutter located between the source and chamber window. A. O. Smith Model A2500-10 SP selectum rectifier power supplies are used in conjunction with external ballast resistors to provide a stable operating current for the arc as shown in Figure 7. A precision shunt located across the power supply allows measurement of the arc current while the electric field strength is measured from the voltage gradient of the cascade stack.

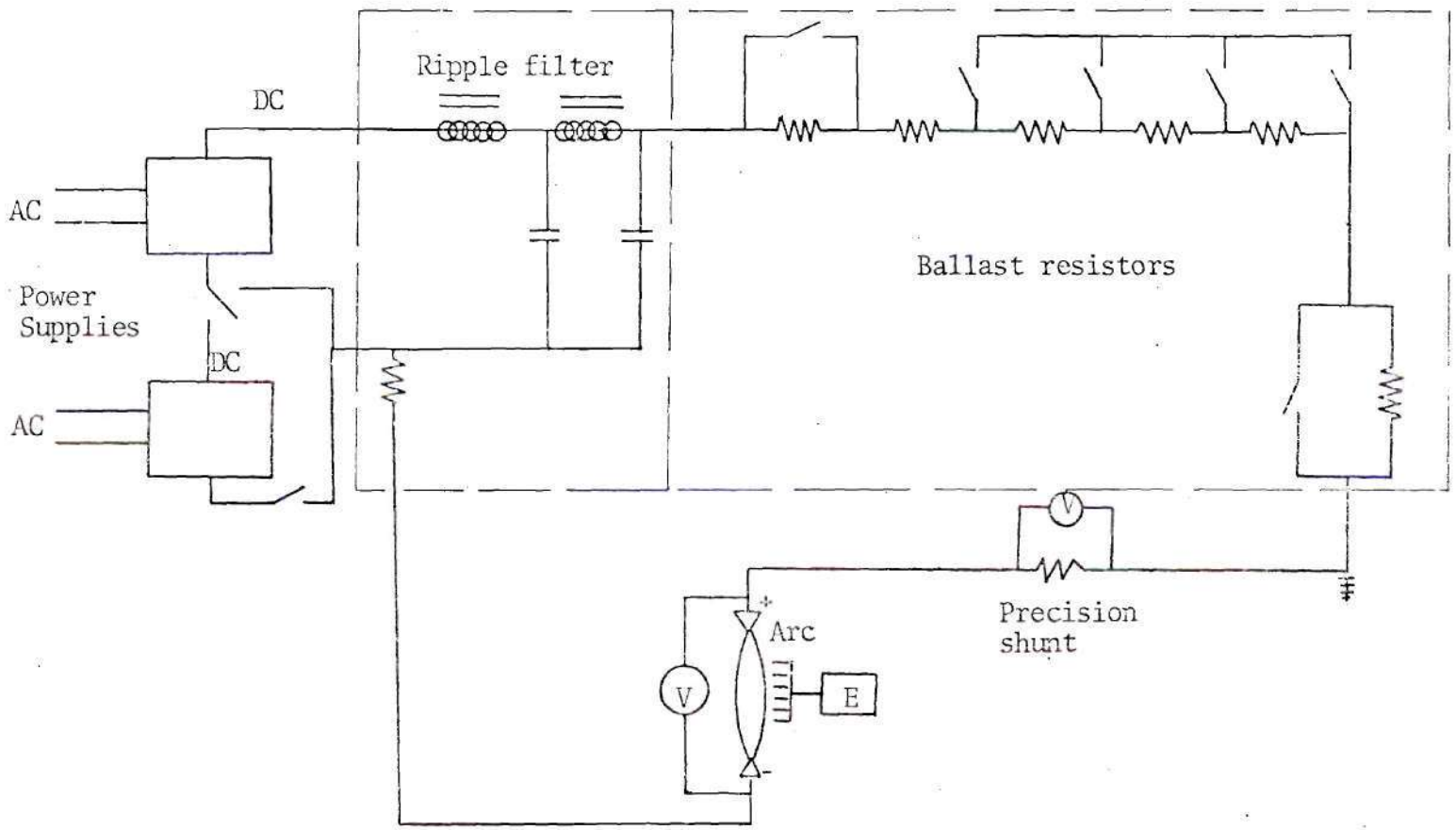

Figure 7. Power Supply System

CHAPTER IV

ASSEMBLY PROCEDURE

The cascade arc is the core of the experimental apparatus. The assembly of the cascade, insertion into the chamber, optical alignment, deaeration and deionization of the water supply, and electrical calibrations are required before the arc can be ignited for experimental purposes.

The cascade is assembled by stacking the plates and their respective gaskets on the cathode manifold as shown in Figure 8a,b. The arc and water channels are aligned with centering pins as the cascade is stacked and torqued to provide proper plate spacing and sealing of the gas and water gaskets. The cathode assembly is mounted on the lower manifold with the electrode aligned on the arc channel axis.

The cascade assembly is installed in the pressure vessel insert with the gas, electrical, and water connections passing through the end plugs. Protective copper shroud is placed around the vessel assembly and the complete apparatus is secured in the chamber. The chamber is purged with argon and the water system is deaerated and deionized in preparation for the experiment.

The optical axes of the spectrometer and cascade

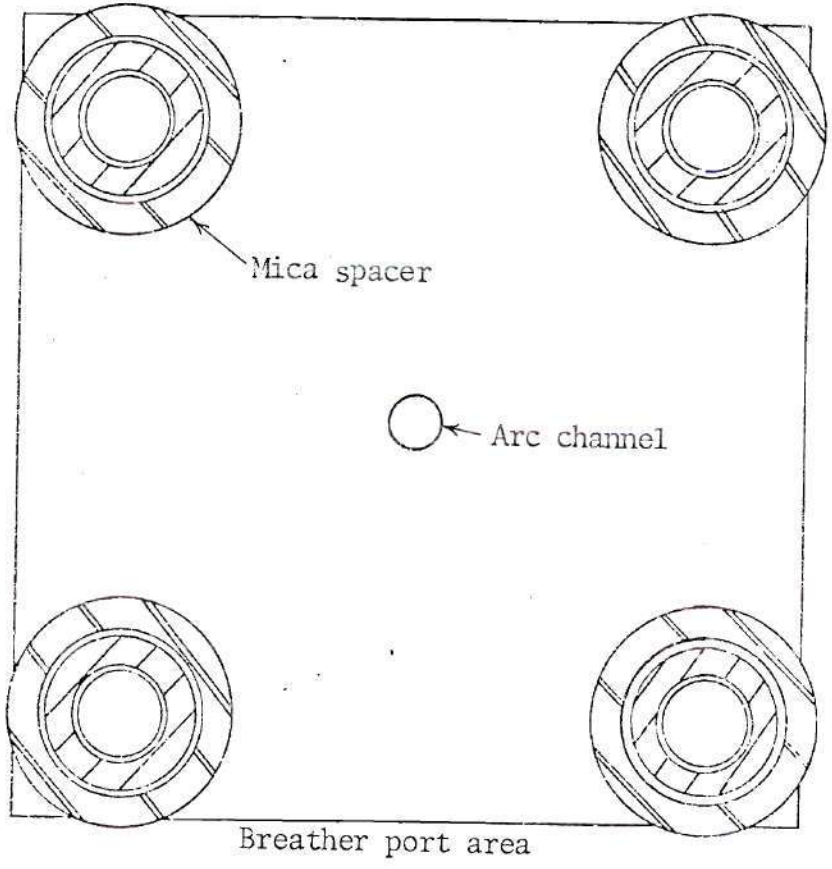

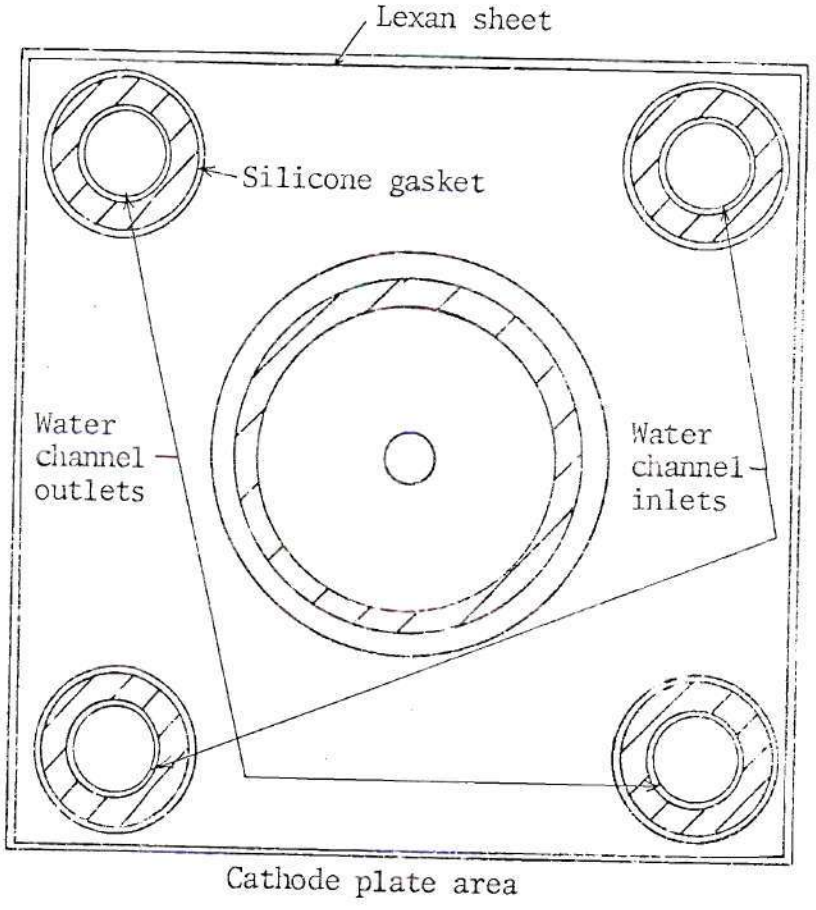

Figure 8a. Various Cascade Plate Areas

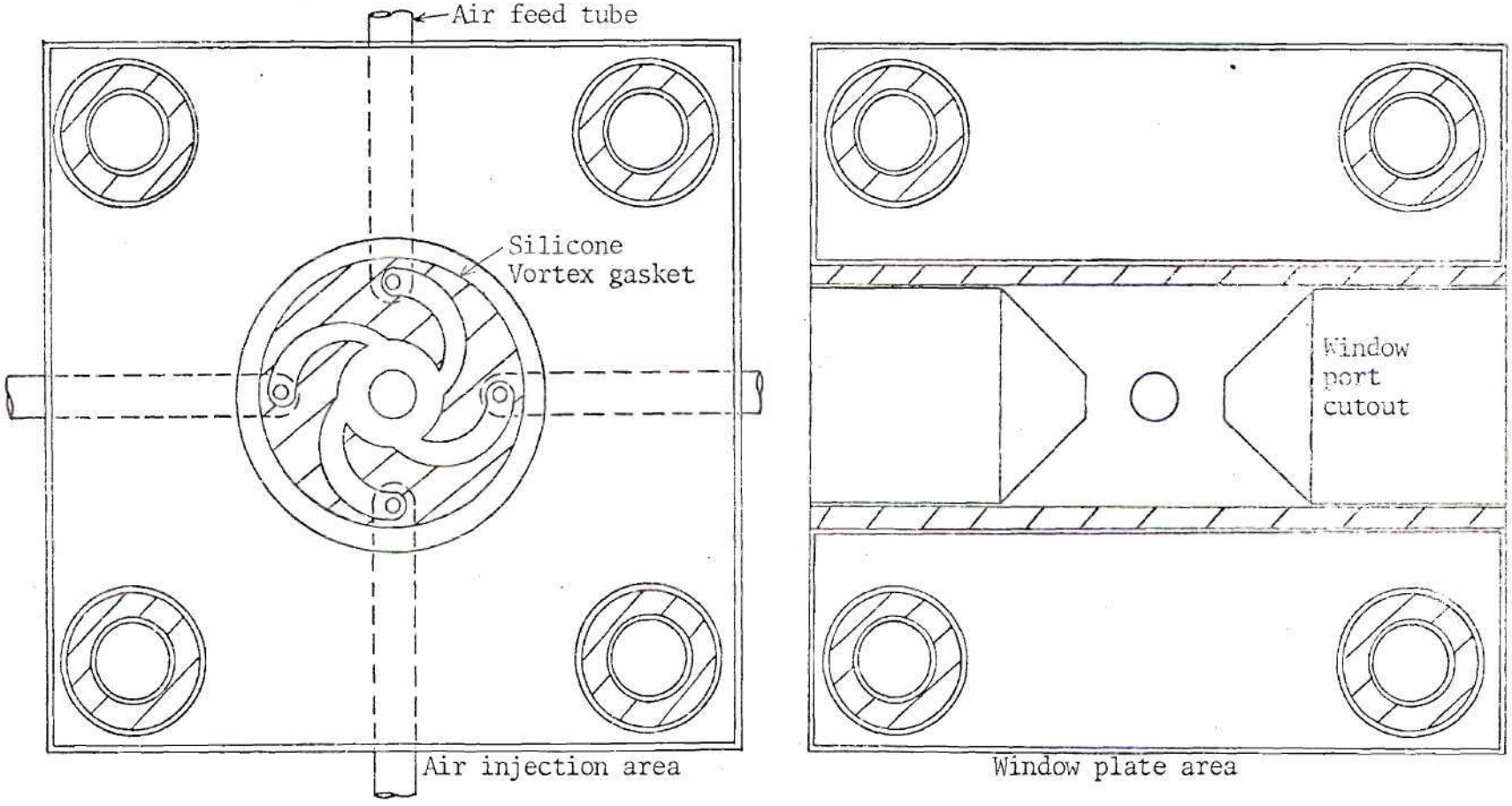

Figure 8b. Various Cascade Plate Areas

window area are aligned in the same horizontal plane at 90° as is shown in Figure 6, by a 632.8 nm laser beam traversing the spectrometer in the reversed direction. The lens is inserted normal to the optical axis and the stand is adjusted so that the lens axis remains aligned with the optical axis as it traverses the optical bar. The vertical axis of rotation of the front surface mirror is inserted normal to the horizontal axis at the intersection of the spectrometer and window area axes.

The cascade window area is aligned to the horizontal plane so that an optimum intensity symmetrical diffraction pattern is obtained as the laser beam is scanned across the optical path to each side of the arc. The leading edge of the chopper blades are aligned with the window area so that the backlight is uniformly chopped across the optical path. The focus of the arc axis is obtained by adjusting the lens position to focus the image of a backlighted calibrated rod, inserted through the anode bore, on the spectrometer entrance slit.

The initial position of the mercury lamp is obtained by aligning the electrode with the laser beam passing through the cascade channel axis. The horizontal and vertical position of the lamp are then adjusted to obtain the maximum signal at the arc center with a symmetrical backlight intensity distribution across the optical path as shown in Figure 9a. The beamshifters are inserted with their axes

of rotation normal to the optical axis and in the same horizontal plane. Their angle of rotation is adjusted to provide a peak signal on the spectrometer. The calibrated rod is inserted and the spatial transmission is obtained from both recorders to allow calibration of the strip charts to distance as shown in Figure 9b.

The electronic system is allowed an hour to reach equilibrium condition in the room at a controlled temperature. Electrical calibration of the various amplifiers and deionization of the cooling system are final steps in the apparatus preparation procedure.

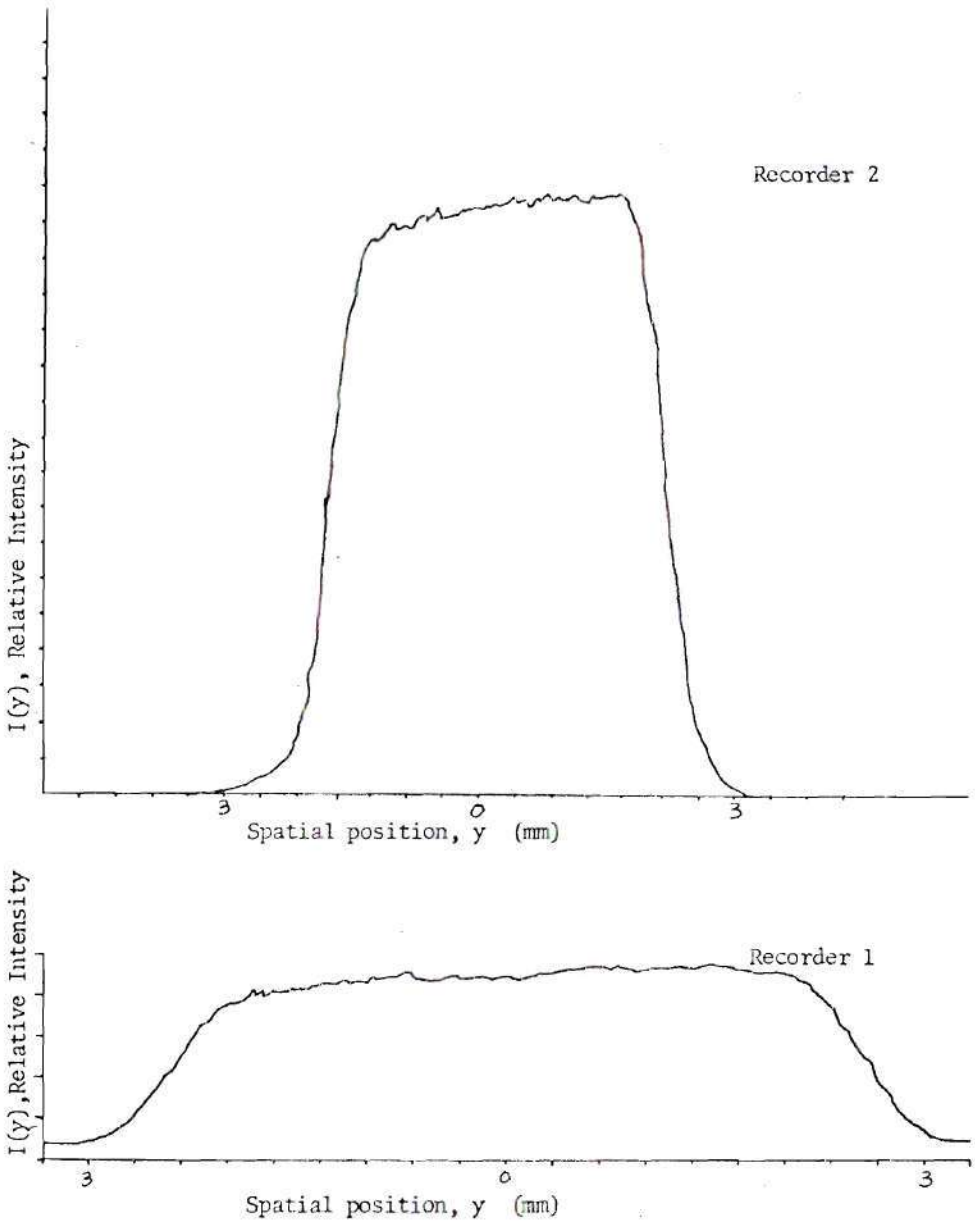

Figure 9a. Spatial Intensity Distribution of Mercury Lamp, λ= 546.4 nm.

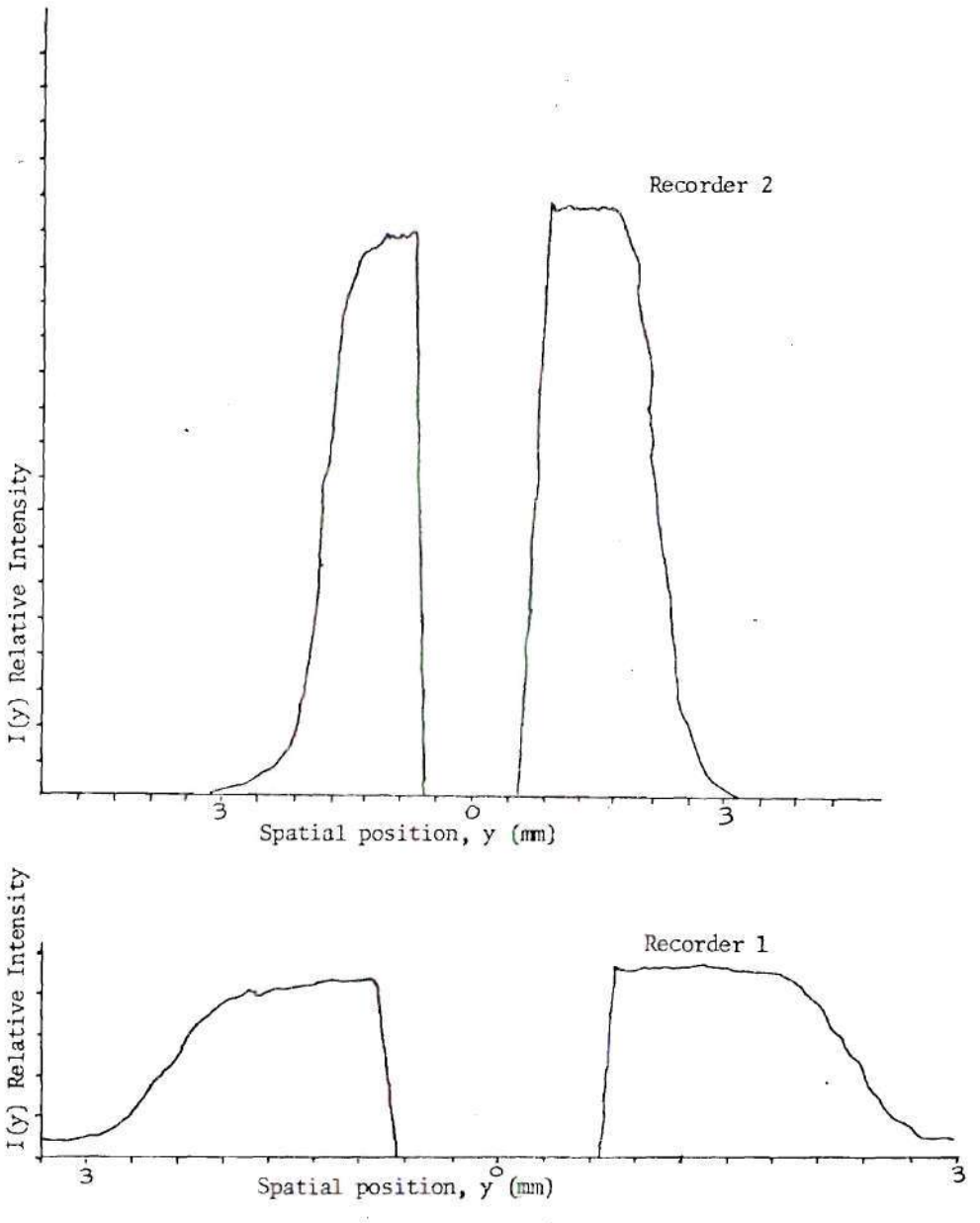

Figure 9b. Spatial Scale Calibration

CHAPTER V

EXPERIMENTAL PROCEDURE

Preliminary spectral scans of the mercury lamp emission were taken to allow for the selection of strong lines for transmission studies. The compensators at the lamp and also at the spectrometer were set to provide the maximum signal at a wavelength of 632.8 nm. The spectrometer entrance and exit slits were adjusted to provide a spatial resolution of 2.5% of the arc diameter and a spectral resolution of .067 nm. The spectral emission was taken at the channel axis from 300.0 to 900.0 nm as shown in Figure 10.

The mercury line at 546.35 nm was selected for the measurement of the absorption effects of cold argon gas (the arc environment) at pressures of 1, 10, 30, and 100 atmospheres. The chamber assembly was charged to the desired pressure (with the arc off) and allowed to stabilize until no schlieren effects were present in the optical path. The lamp signal was monitored at the channel axis as beamshifters 2 and 1 were adjusted for optimum signal. Spatial transmission scans across the optical path were simultaneously plotted on both recorders as shown in Figures 11a and 11b.

The emission spectra of argon and air arcs were obtained next at various pressures to survey the lines

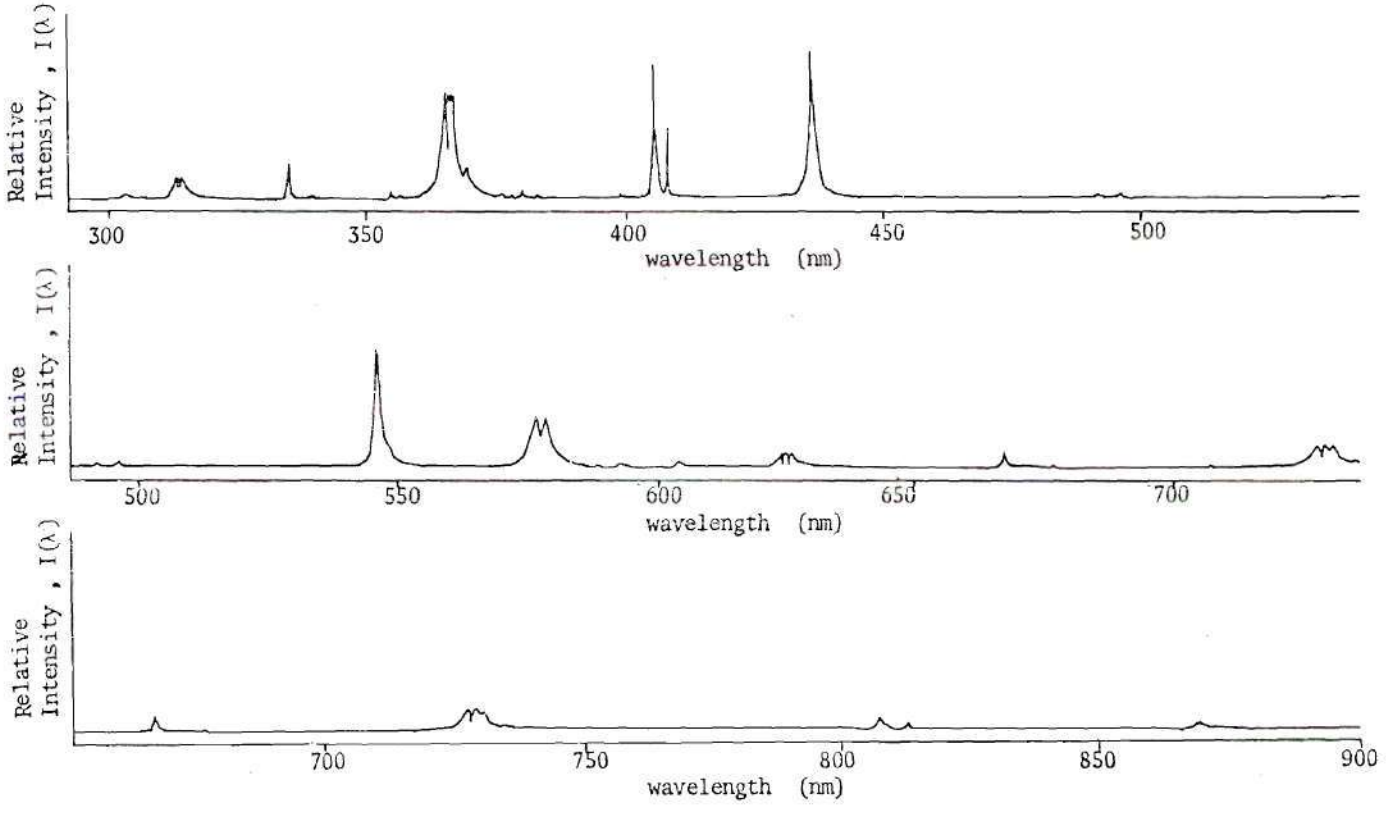

Figure 10. Mercury Lamp Emission Spectra , Recorder 1

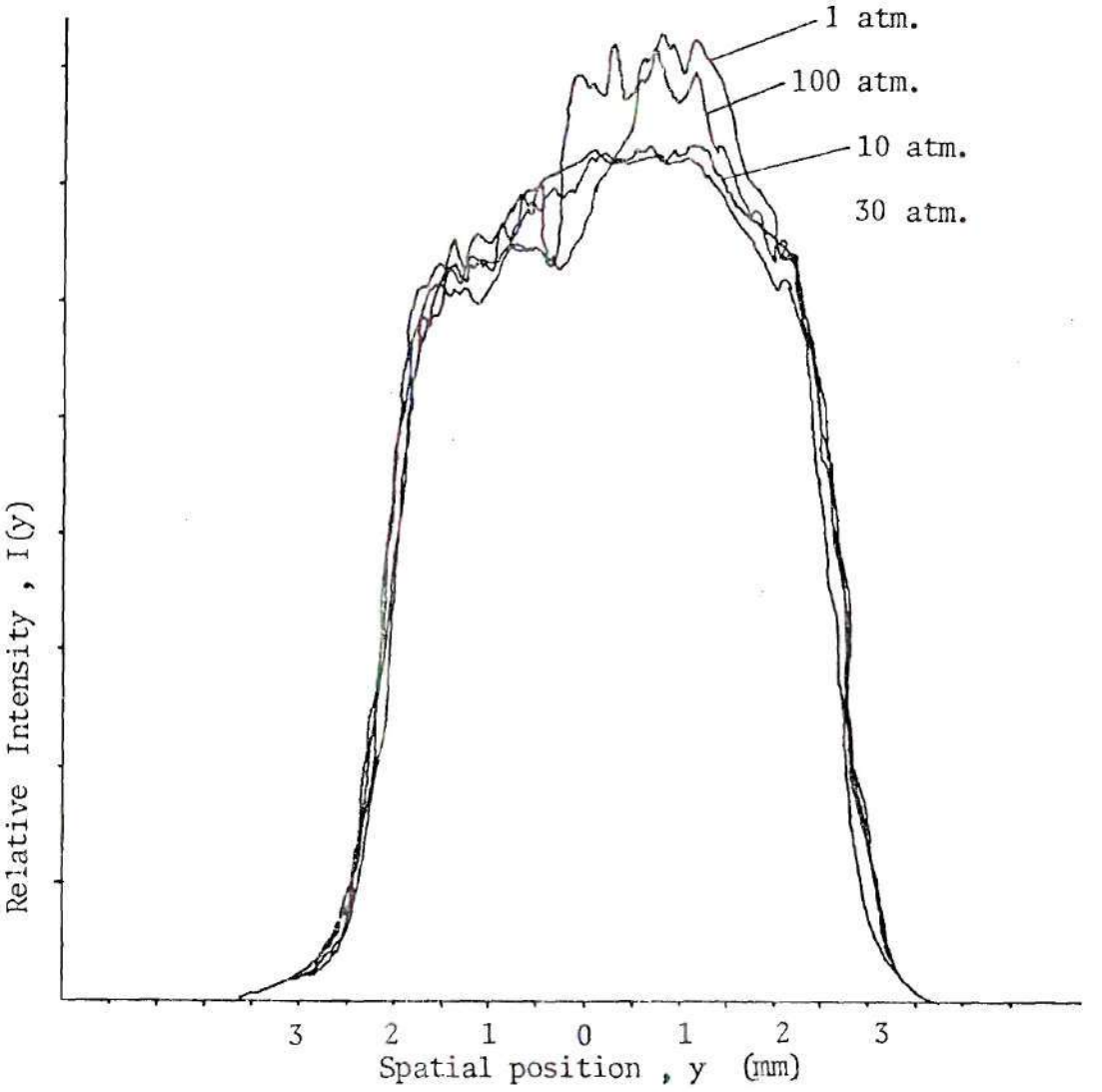

Figure 11a. Cold Argon Gas Transmission, Recorder 2

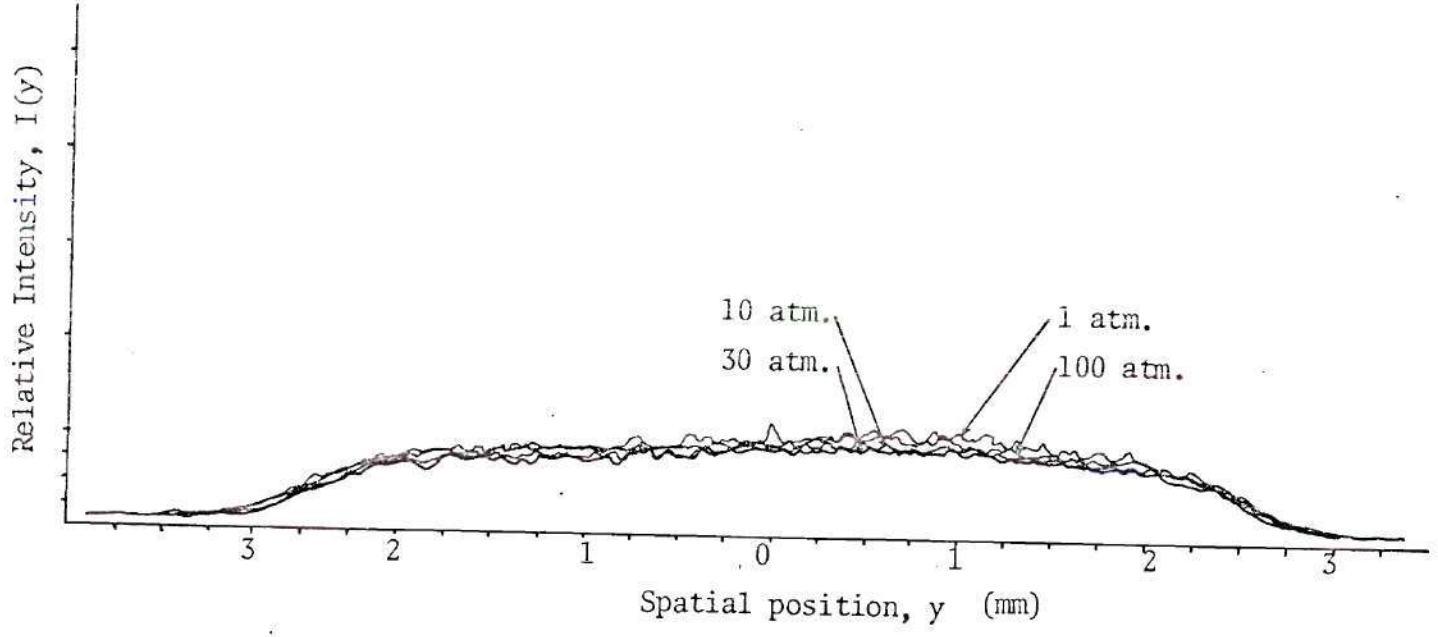

Figure 11b. Cold Argon Gas Transmission , Recorder 1

applicable to temperature determination. The pressure chamber was filled with argon at one atmosphere, the cathode and anode flows were established, and the cooling system was isolated from the deionizer as the water pump and heat exchanger were activated. The arc was struck by the extraction of a tungsten rod which draws the arc from the cathode to the anode. The vent area and chamber were sealed and the high pressure area of the laboratory was cleared of personnel.

The argon emission spectra were obtained at pressures of 1, 30, and 100 atmospheres. The arc pressure, current, and electrode flows were adjusted as their interactions were allowed to establish an equilibrium condition. The spectrometer, picoammeter, and recorders were adjusted to provide the desired line amplitudes and spectra resolution. Spectral scans from 350.0 to 900.0 nm were obtained during equilibrium conditions at various pressures as shown in Figures 12 and 13a,b.

The air emission spectra were then obtained at pressures of 1, 10 and 30 atmospheres. A stable argon arc was established and optimized at the desired pressure. The air was injected into the test section as the electrode flows and vent rate were adjusted to maintain a stable arc at the desired pressure. The ArI 840.8 nm and 842.4 nm lines were compared to the OI 844.6 nm line at the arc center as the air percentage increased with injection rate.

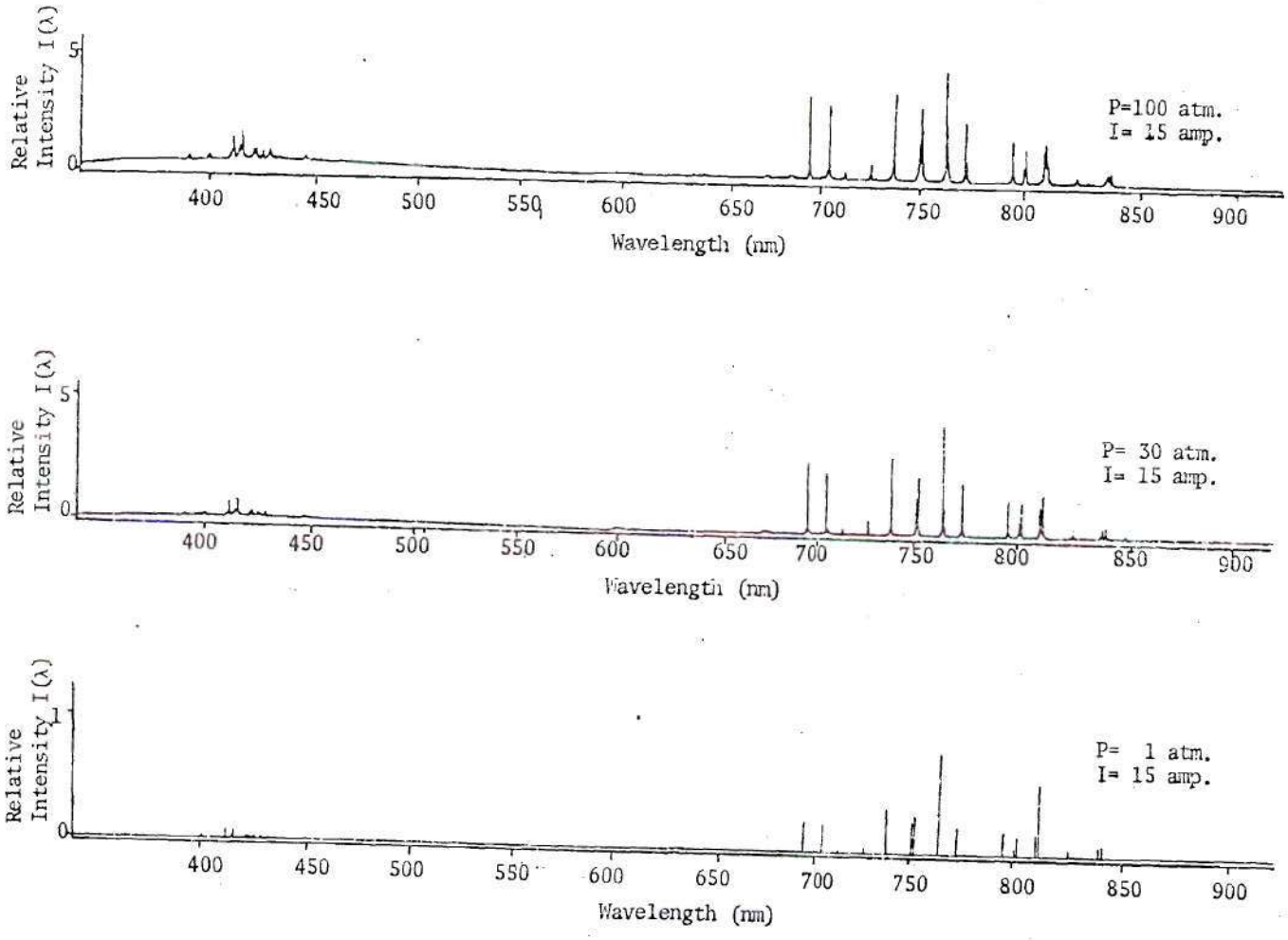

Figure 12. Argon Emission Spectra 350-900 nm.

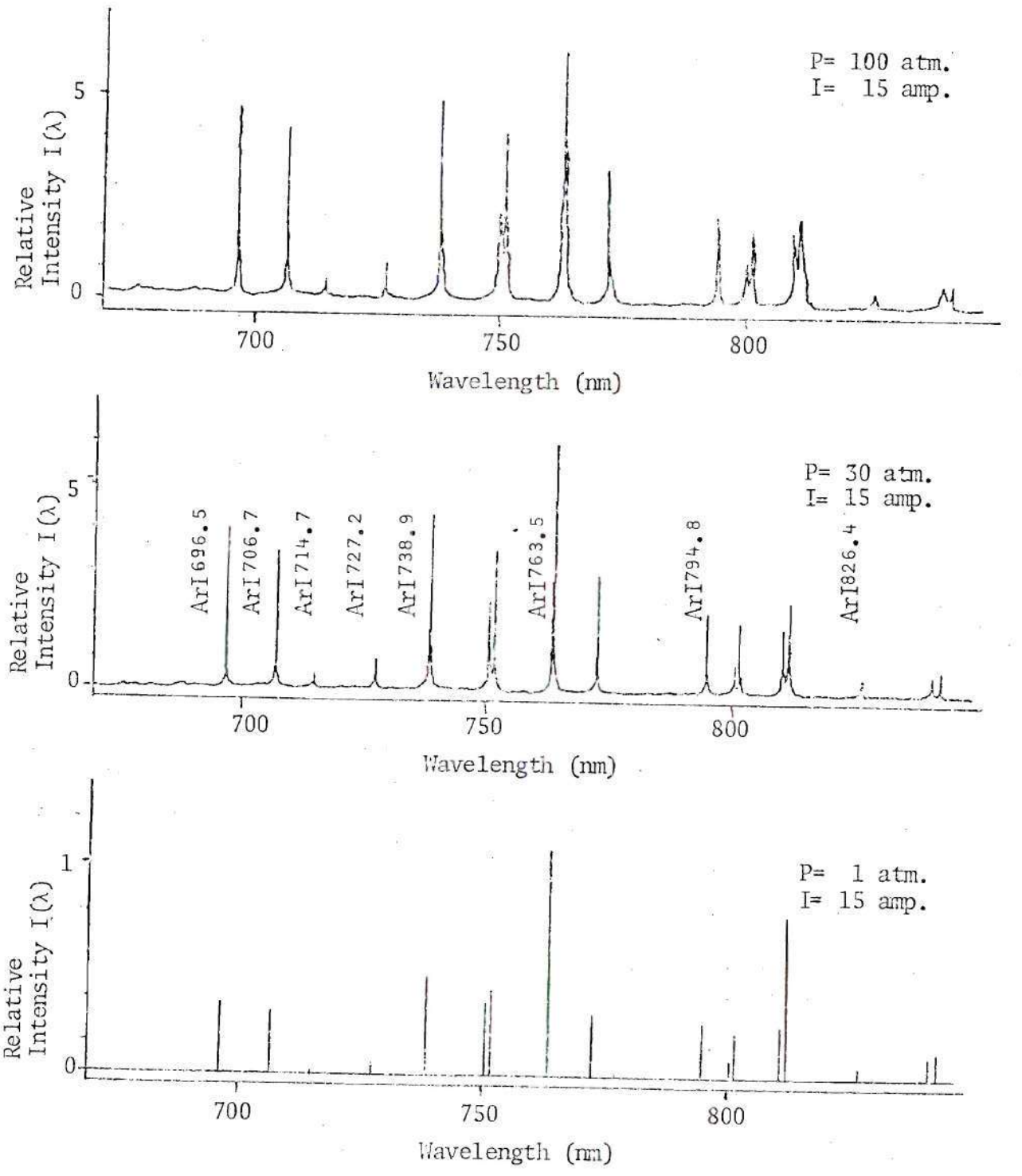

Figure 13a. Argon Emission Spectra , 650-850 nm.

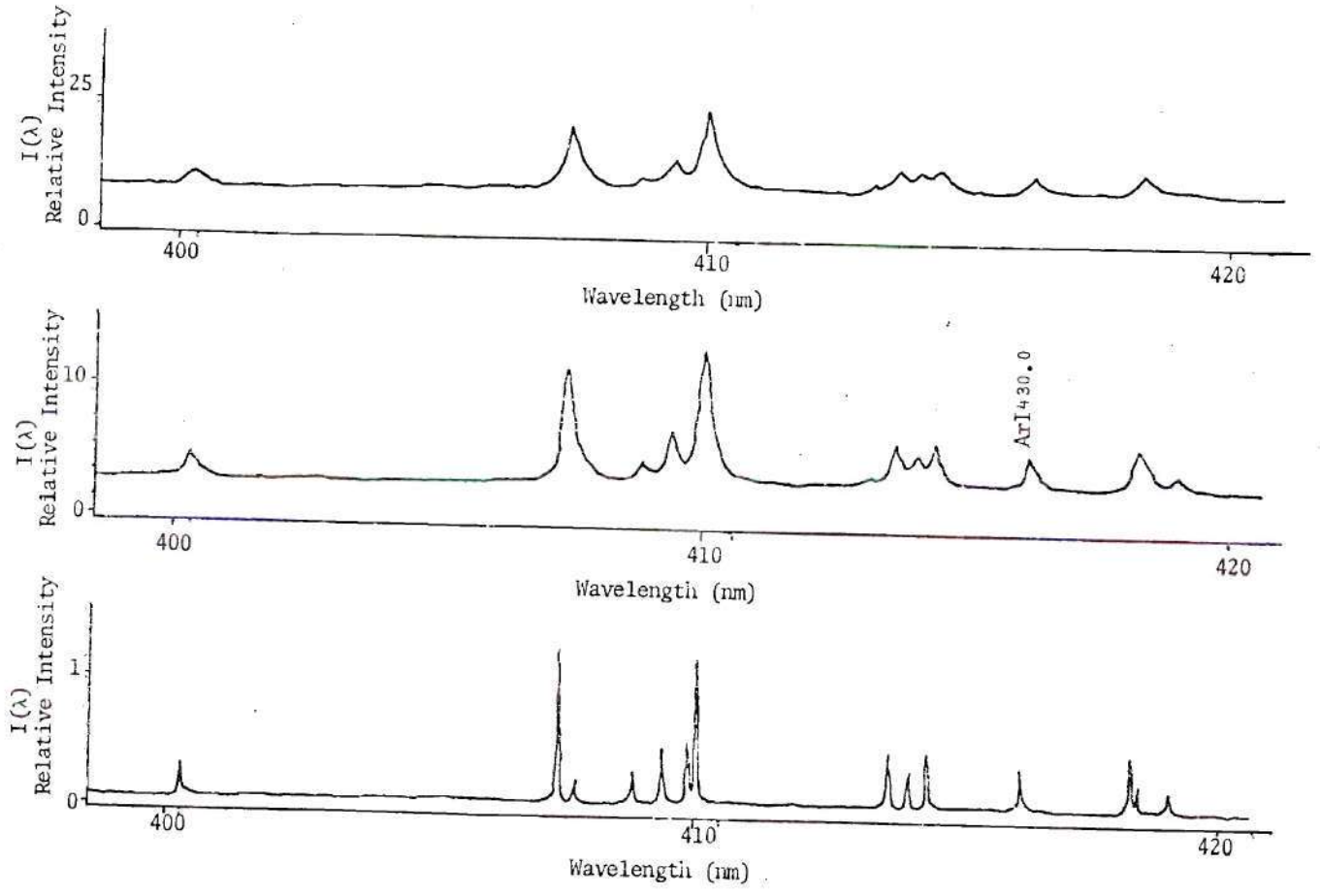

Figure 13b. Argon Emission Spectra 400-450 nm.

Air purity was obtained when the argon lines were no longer observable and the oxygen line had reached a peak amplitude with the injection rate. The arc current, flows, and pressure were allowed to stabilize as the arc center was monitored for purity. These spectra were obtained at various pressures at wavelengths from 600.0 to 850.0 nm as shown in Figures 14a,b,c,d. The presence of the ArI lines in the air emission spectrum indicates that either air purity was not established during the entire spectral scans, or the ArI 840.8 and ArI 842.4 nm lines are relatively weak emitters as compared to the lines present such as the ArI 763.5 nm line.

The spectral absorption through the vessel with an operating argon arc was investigated at a pressure of 30 atmospheres and an arc current of approximately 13 amperes. The mercury lamp 546.4 nm line was used to backlight the optical path across the arc channel and window plate gap areas as shown in Figure 15. The 30 atm argon arc has absorbed and refracted the mercury backlight signal as seen in Curve 2 of Figure 15. The symmetry consideration of the geometry of this region as seen in Figure 18b led to the conclusion that the signal loss effect occuring in the left region of the plate gap area should be similar to the effect in the right region. Hence the mercury lamp was laterally repositioned to improve the illumination of the left plate gap area while maintaining the illumination of the arc channel area. The result is shown as Curve 3 in Figure 15. The

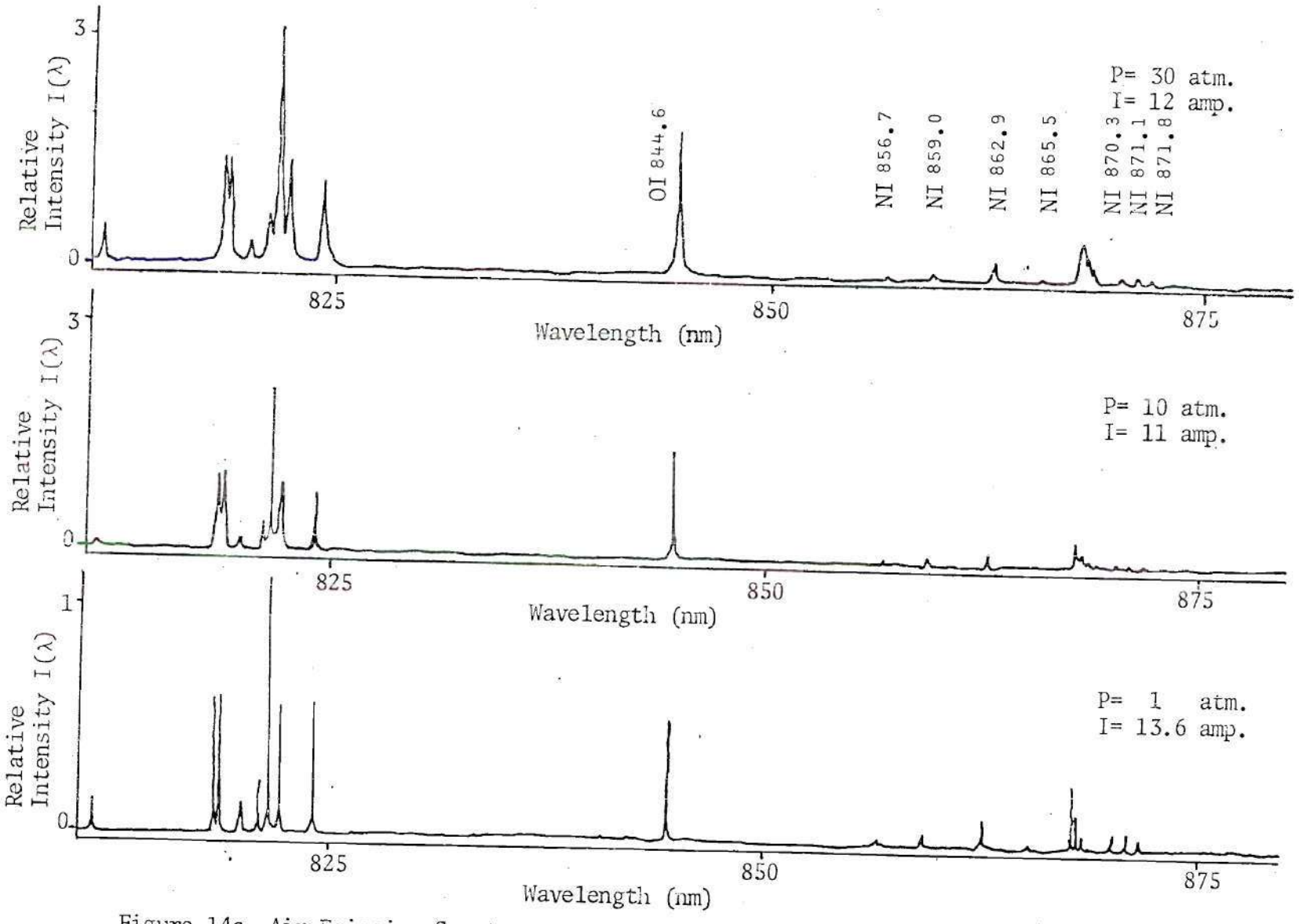

Figure 14a. Air Emission Spectra

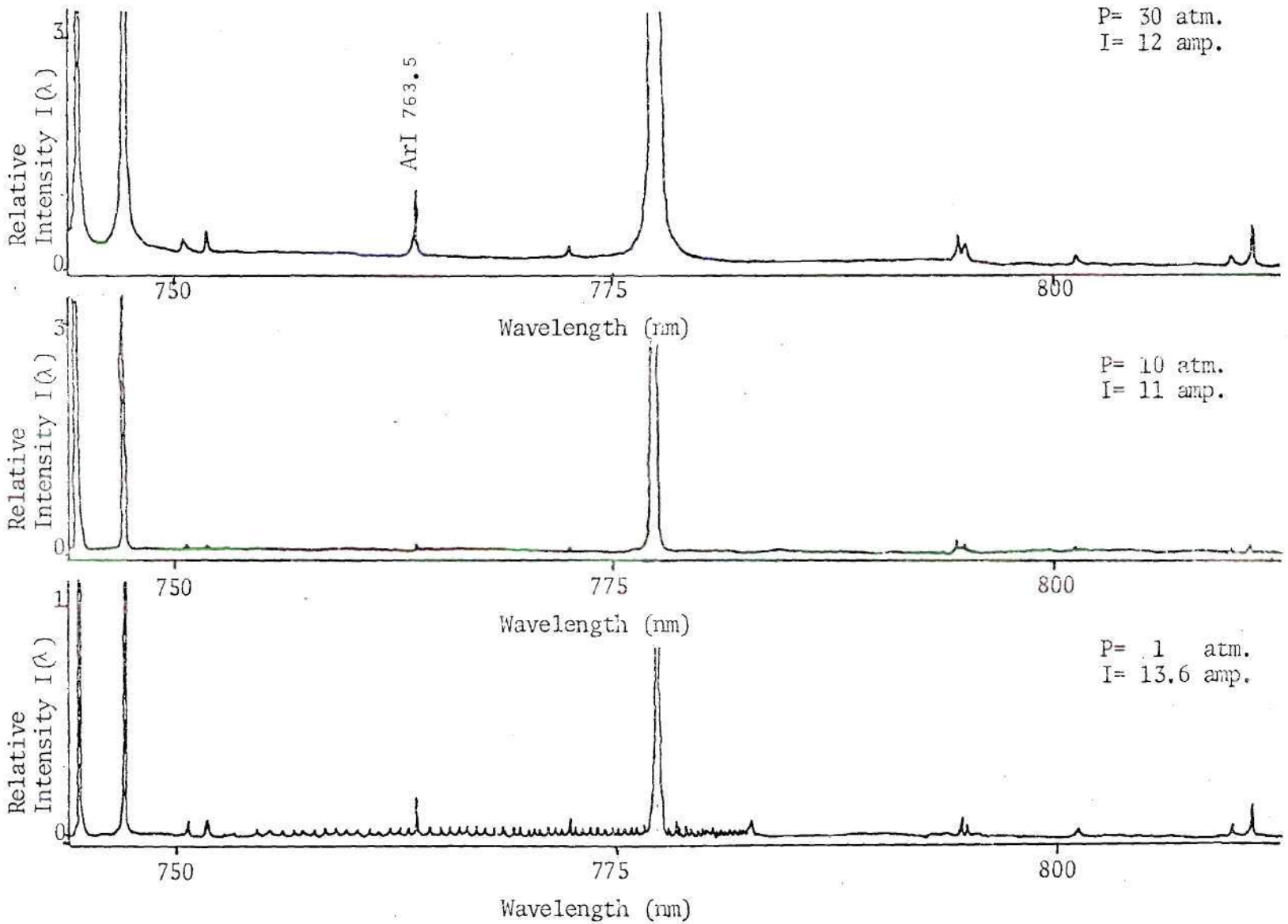

Figure 14b. Air Emission Spectra (cont'd)

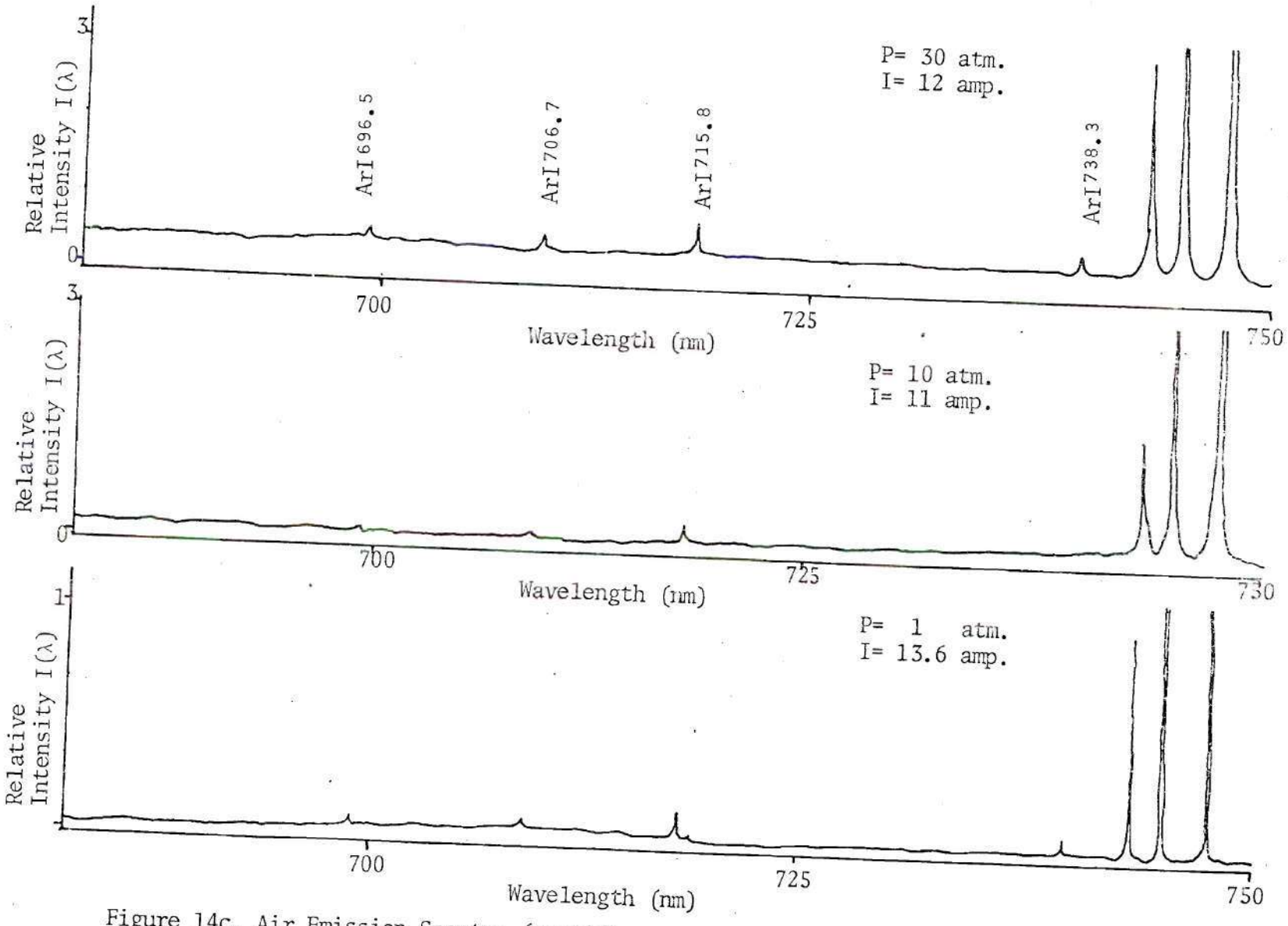

Figure 14c. Air Emission Spectra (cont'd)

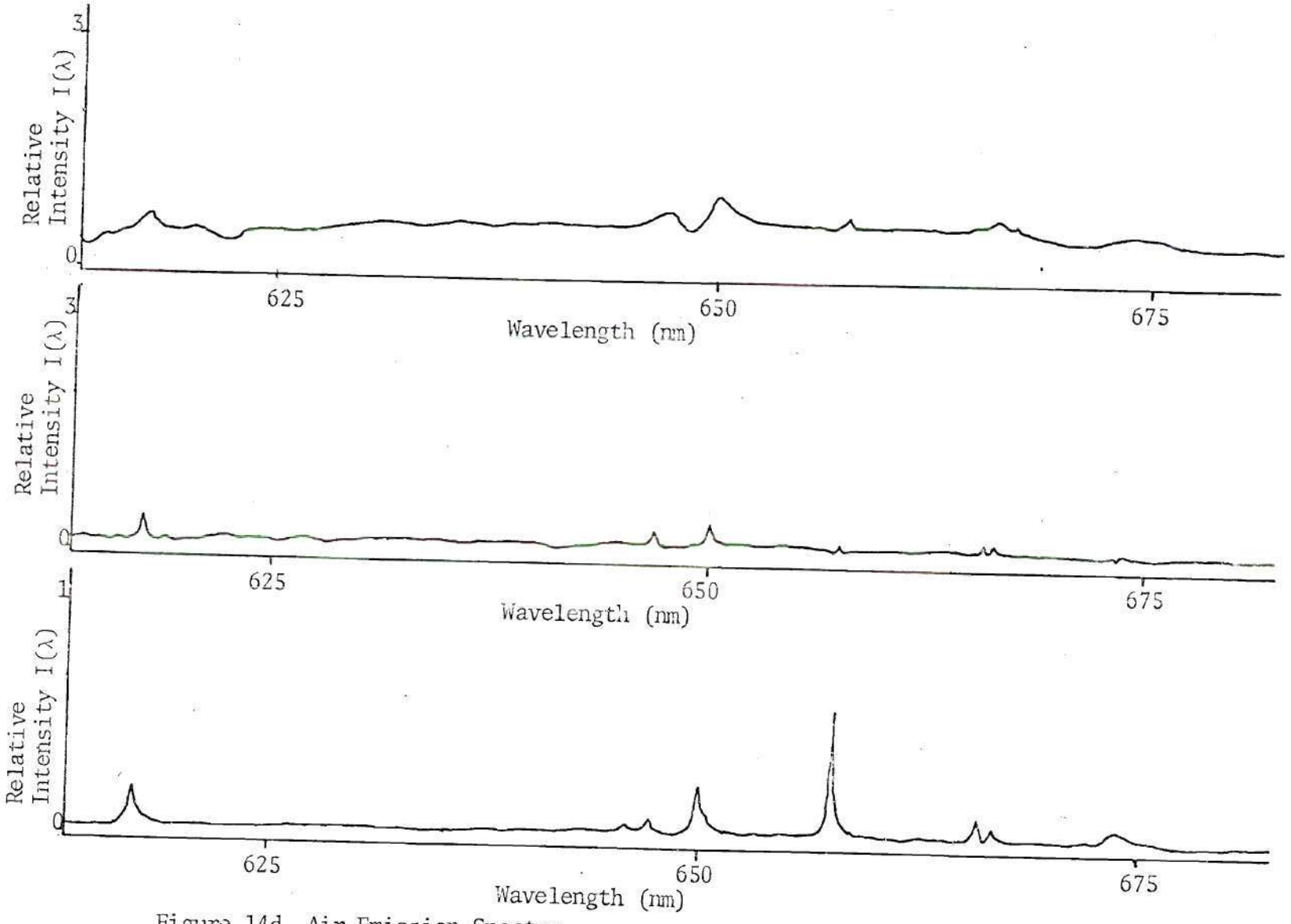

Figure 14d. Air Emission Spectra

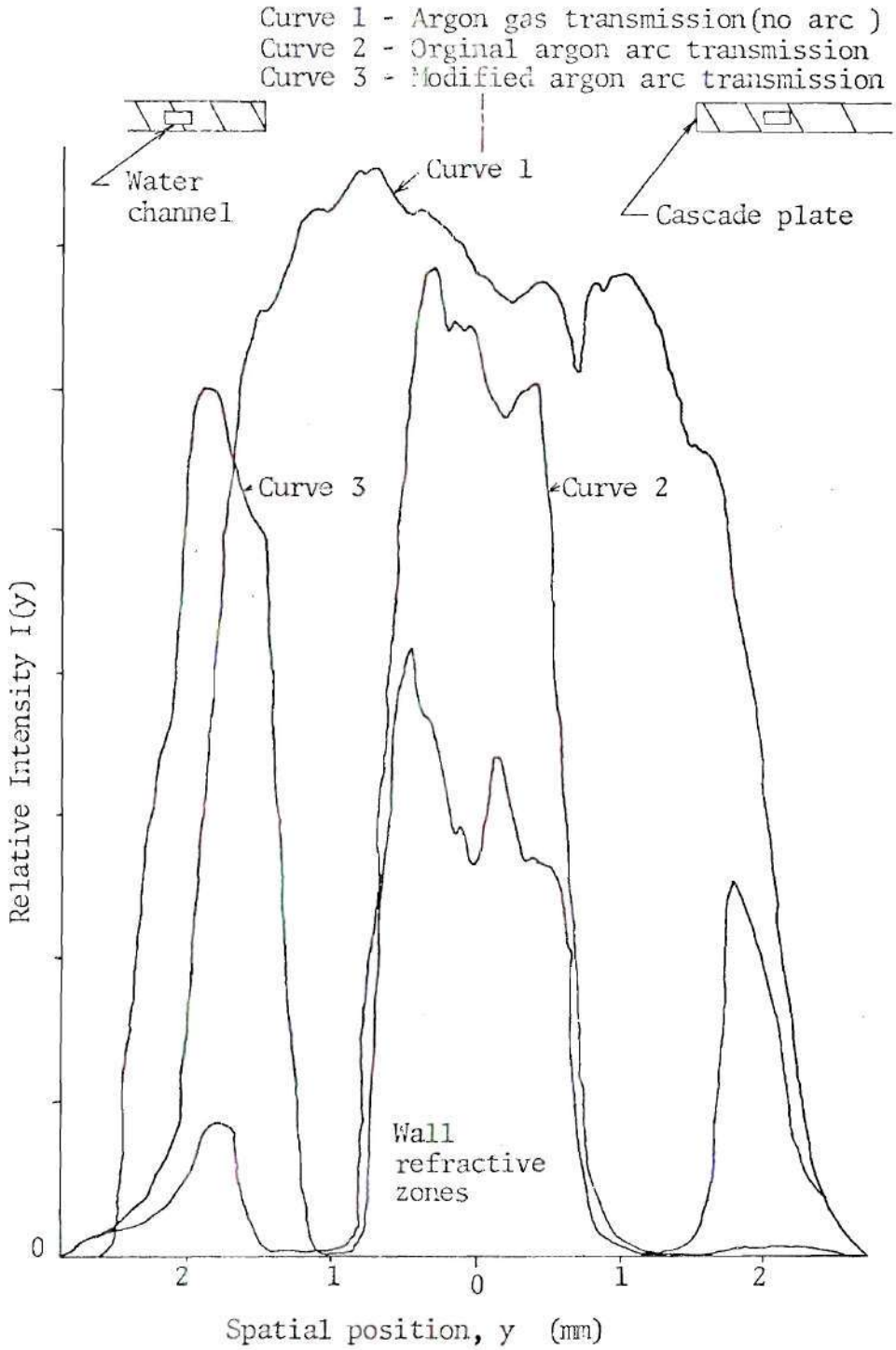

Figure 15. Argon Arc Transmission and Refractive Effects at 30 atm.

apparent drop in the central region was corrected by a beamshifter.

The argon arc transmission as seen in Figure 16 was monitored by the chopped technique on Recorder 2 as air was injected in step increments into a stable optimized argon arc. The transmission across the optical path was spatially scanned as the electric field strength was used as an indicator of the air percentage in the arc. The transmission was monitored until the transmission had dropped by a factor of 8 at which time the field strength had increased from 22 v/cm to 34 v/cm indicating considerably less air than needed for air purity corresponding to 70 v/cm. The 30 atm argon arc transmission and air arc transmission as measured by the chopper technique are shown in Figure 16.

The air injection was then stopped and the arc was purged with argon injected from the cathode area. The arc gradually returned to an argon arc as the air percentage decreased and the transmission recovered in the window plate area as the byproducts diffused into the chamber area. For baseline information the spectrum of the mercury lamp as seen through arc center was then obtained from 350 to 600 nm by the chopped technique on Recorder 2 as Spectrum 1 in Figure 17a. Simultaneously, the arc emission spectra were obtained from 420 to 500 nm on Recorder 1 as Spectrum 1 as seen in Figure 17c, and from 820 to 860 nm in Figure 17b. Note that the arc has a slight trace of air as evidenced by

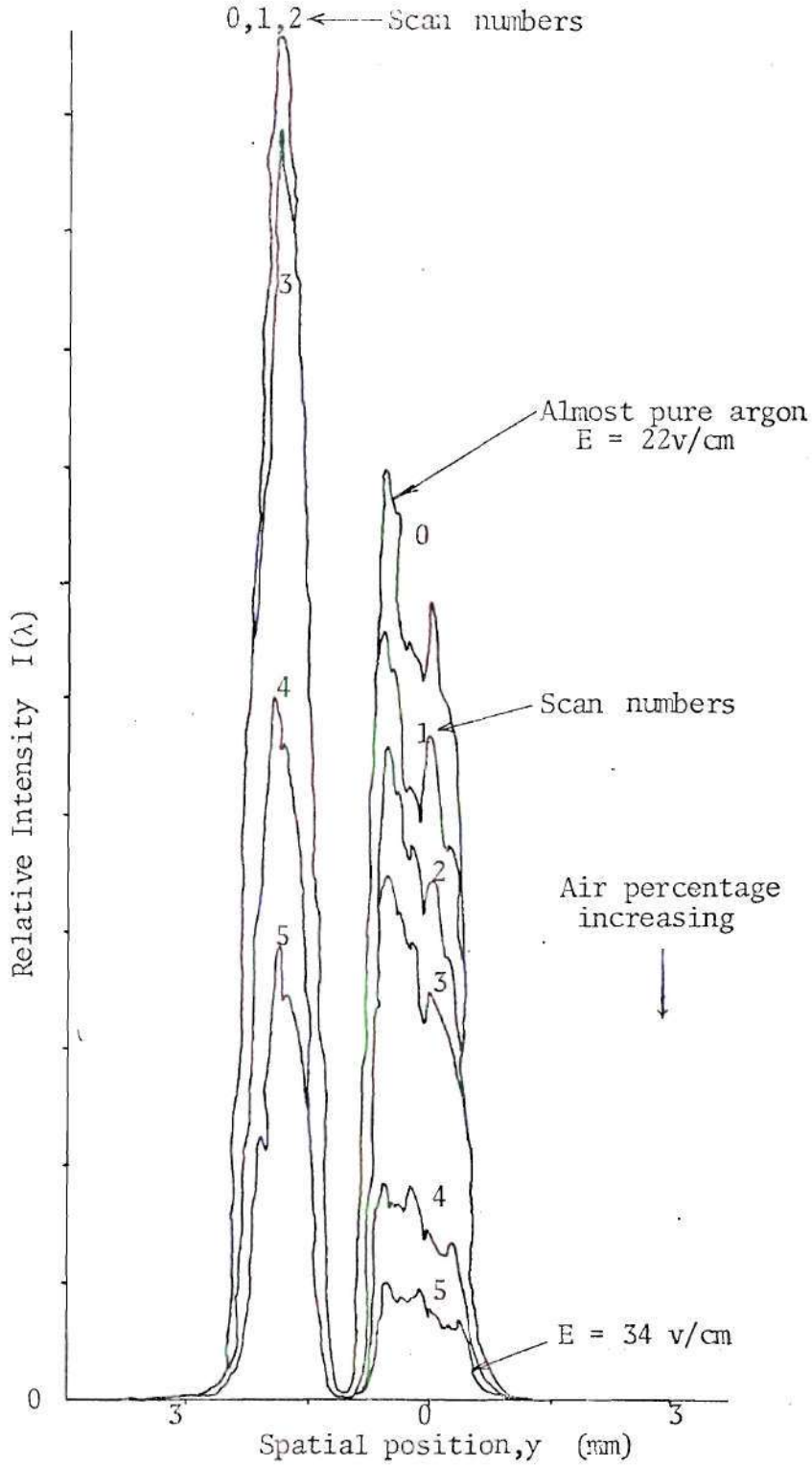

Figure 16. Air Arc Transmission

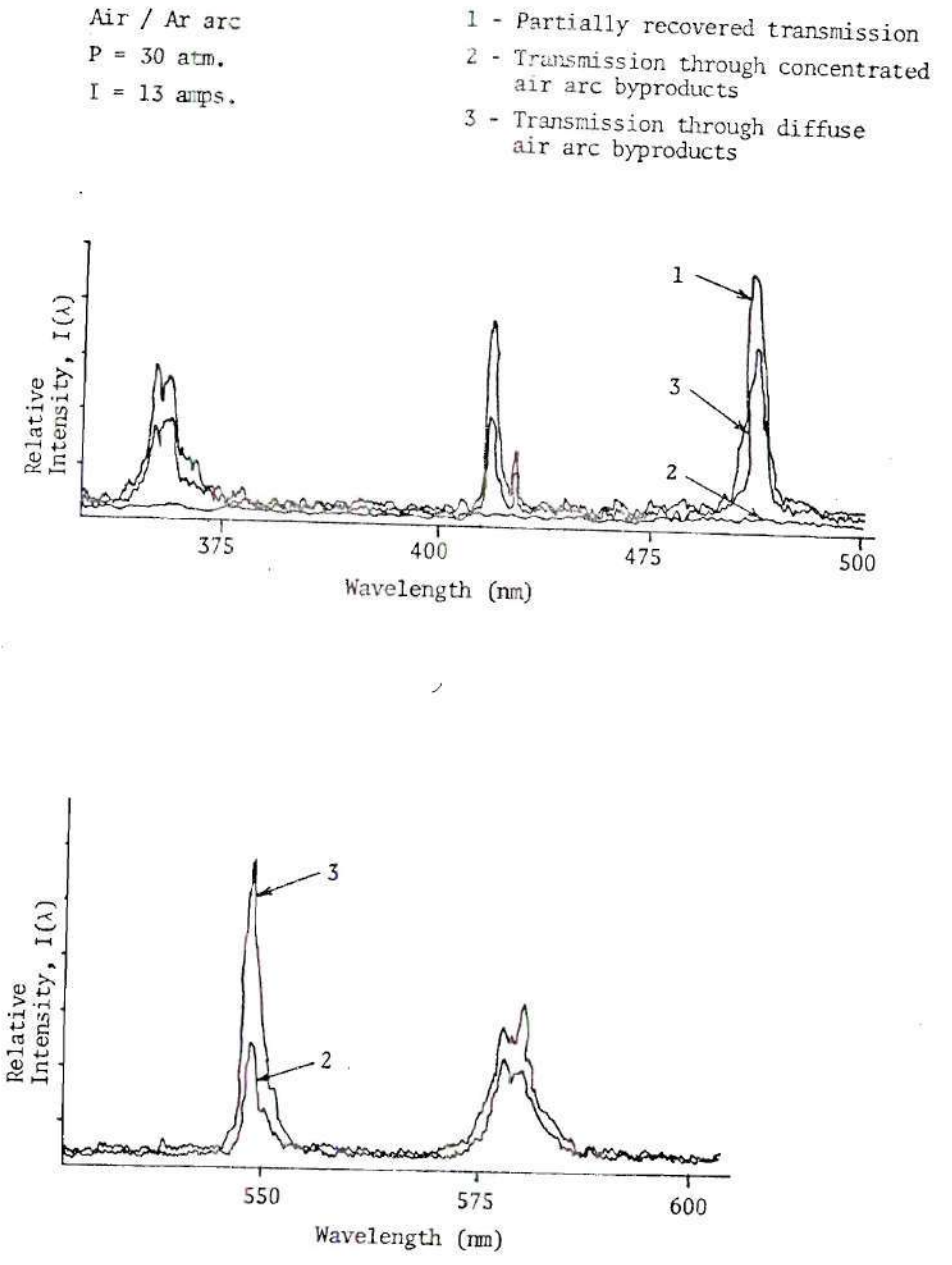

Figure 17a. Relative Transmission Through Arc Center of Hg Lines, Recorder 2

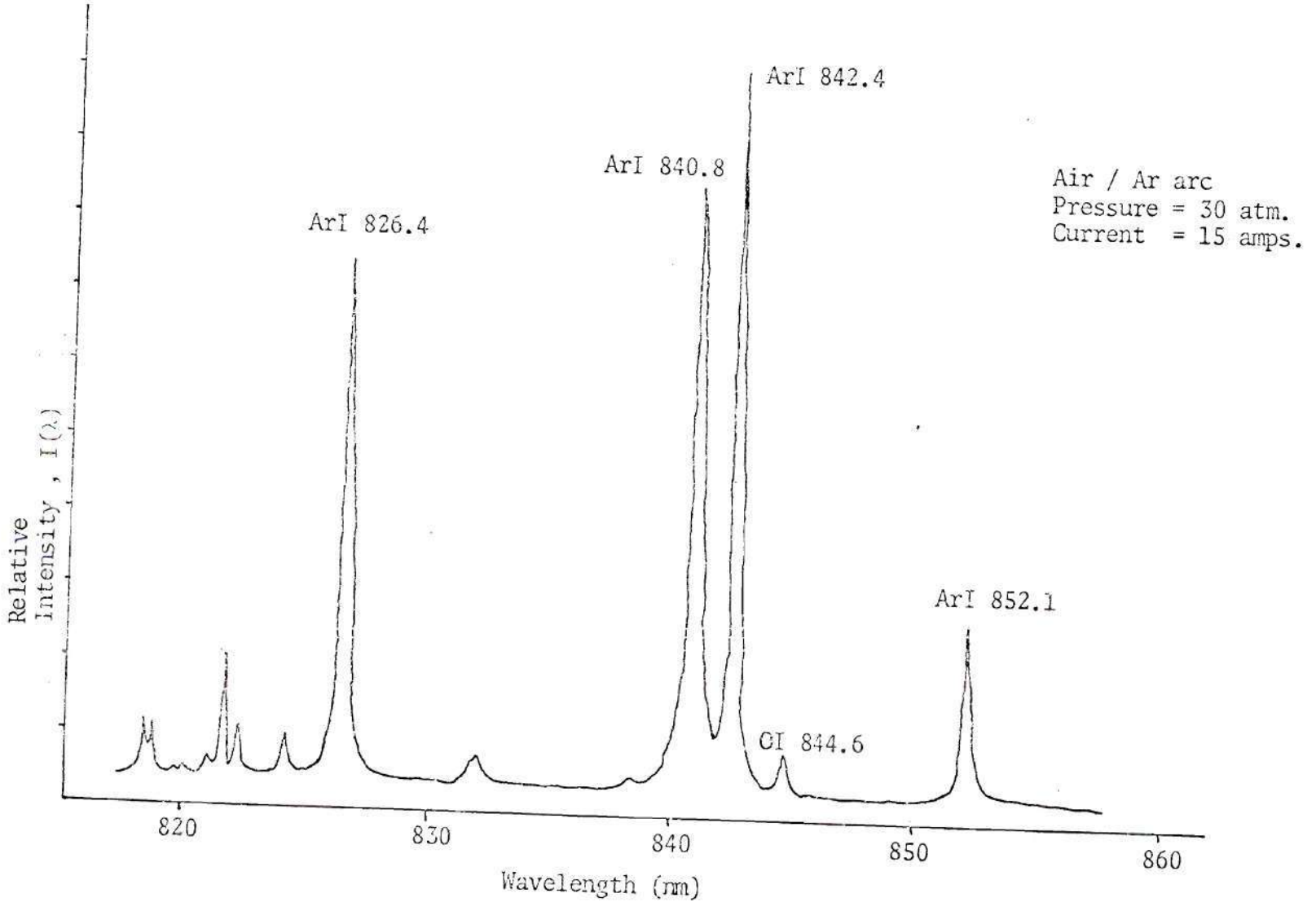

Figure 17b. Air / Ar Arc Emission Through Partially Recovered Medium, Recorder 1

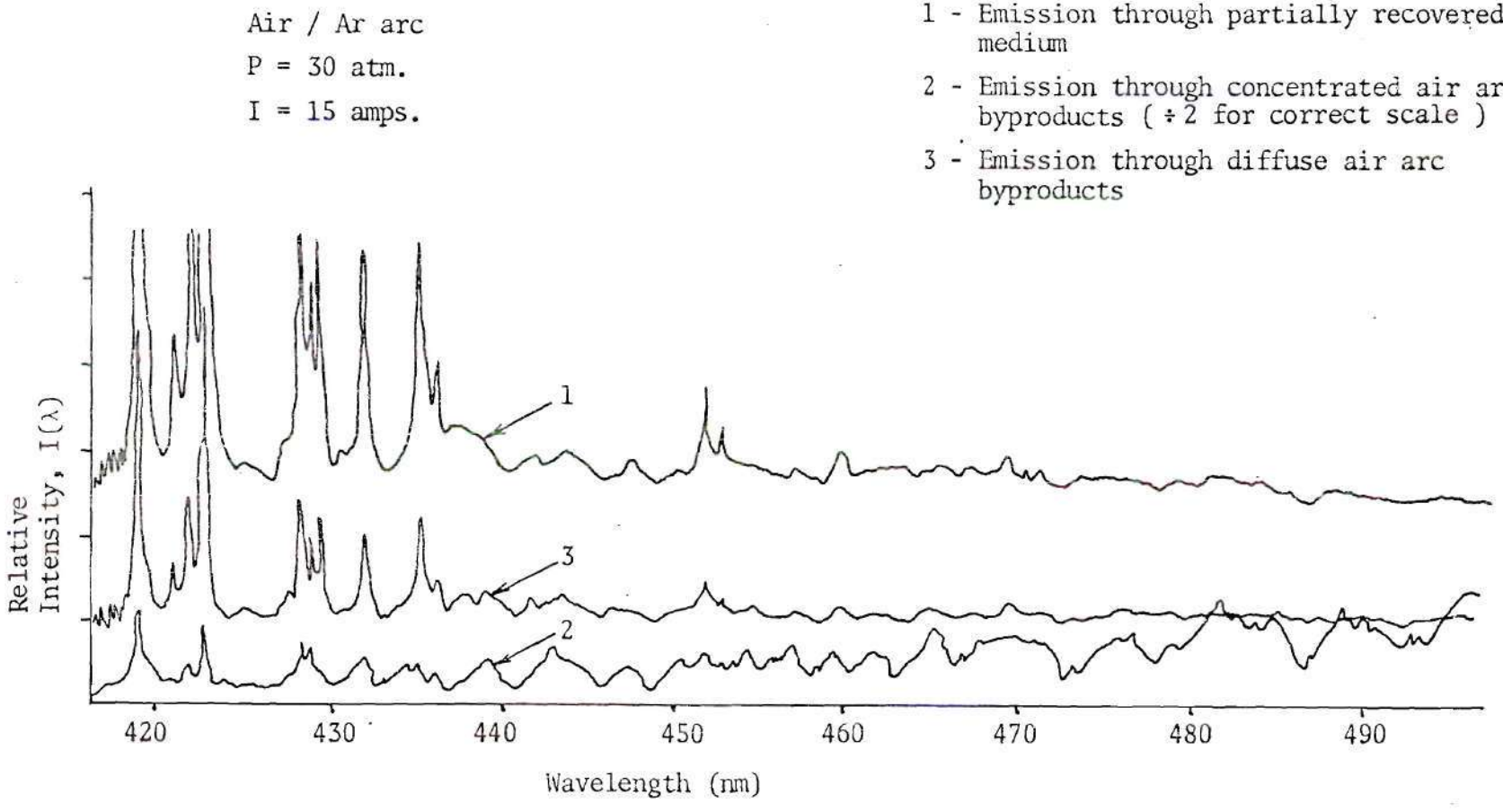

Figure 17c. Air / Ar Arc Emission Through Absorbing Media, Recorder 1

the presence of the OI 844.6 nm line in Figure 17b and that the mercury lamp has no measurable contribution to the arc emission in Figure 17c. A pure air arc was then established and allowed to stabilize for three minutes in order to build up the concentration of byproducts in the window gap area. The arc was then quickly returned to an argon arc with a slight trace of air as the mercury lamp transmission and arc emission were recorded as Spectrum 2 in Figures 17a and 17c, respectively. The argon arc transmission was allowed to recover for three minutes as the byproducts diffused into the chamber area. The mercury lamp transmission and arc emission were again obtained as Spectrum 3 in Figures 17a and 17c.

As seen in Figures 18a,b, the NO_2 absorption spectra from 460 nm to 500 nm shows a one to one correspondence to the measured emission spectrum of the argon arc surrounded by air byproducts. The spectral dependence of the absorption effect caused by the arc products in the optical path was obtained from 300.0 to 900.0 nm along the optical path intercepting the arc axis. An air arc was established and the transmission was allowed to stabilize through the arc center. The air arc was extinguished as the electrode and test section flows were simultaneously stopped. The arc byproducts in the test section were allowed to diffuse into the large chamber area at a steady pressure of 30 atmospheres. Two spectral scans from 300.0 to 900.0 nm were

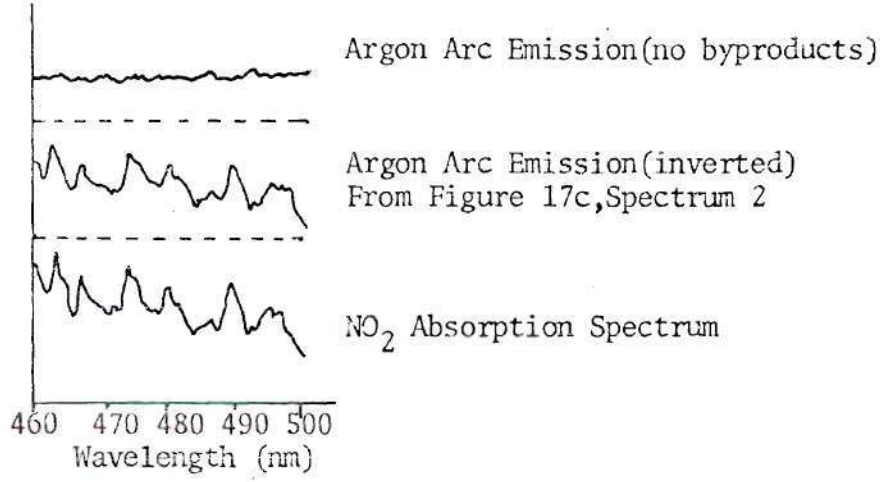

Figure 18a. Air Arc Byproduct Absorption Spectrum vs NO_2 Absorption Spectrum

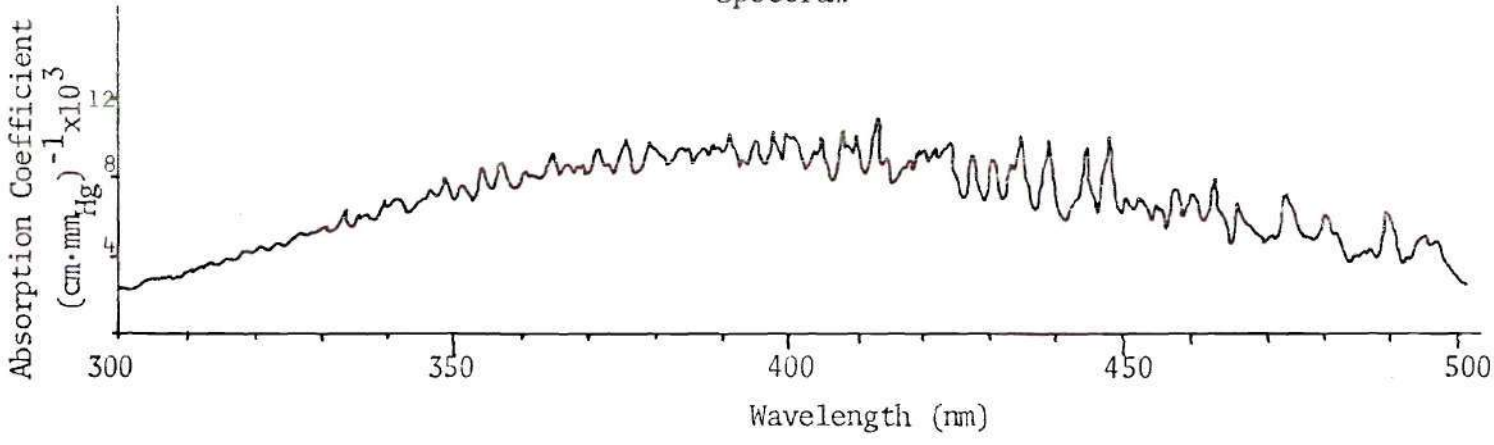

Figure 18b. NO_2 Absorption Coefficient (25°C) From Ref.[20]

obtained in a 15 minute interval in which the transmission recovered to approximately 50% of the baseline signal. As seen in Figure 19, these studies allowed the absorption effects at different wavelengths to be correlated to the previous HgI 546.4 line studies.

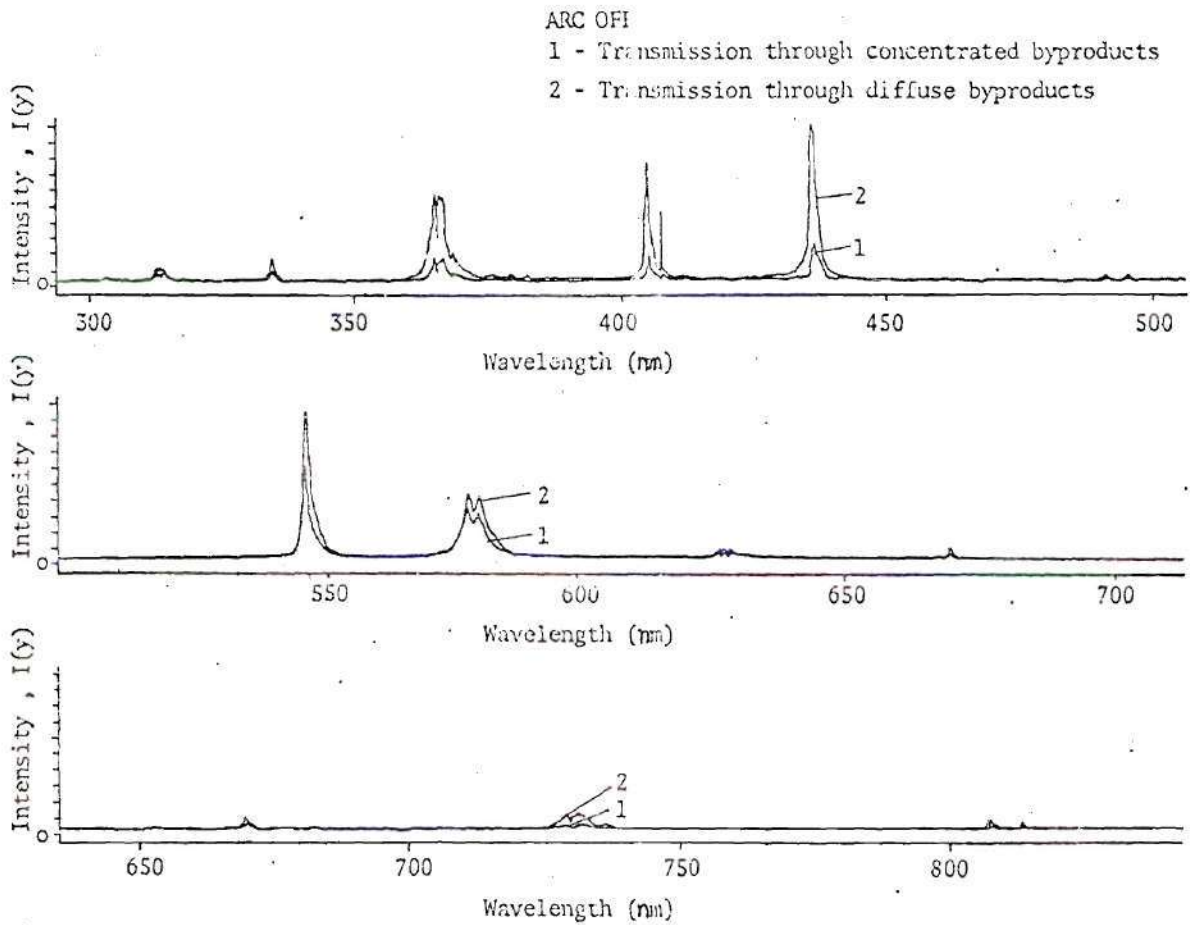

Figure 19. Mercury Lamp Emission Spectrum Through Air Arc Byproducts, Recorder 1

CHAPTER VI

RESULTS

The strong mercury lines for backlighting the optical path are useful in spectral regions in which the arc emission is relatively low. At other wavelengths, the mercury lamp emission is too low for successful absorption measurements.

The HgI 546.4 line was chosen due to its intensity and its central wavelength in the observable spectrum as seen in Figure 10. The spatial scans of the mercury line as seen in Figures 11a,b show that no systematic absorption characteristics exist in cold argon gas at room temperature. The transmission at 1 and 100 atmospheres show higher values across a portion of the scan. No attempt was made to investigate the possible causes, but the lock-in amplifier is suspect.

The emission spectra of argon and air show a variety of lines available for diagnostics as shown in Figures 12 through 14. The experimental error in measurement and the transition probability error as seen in equations 10 and 12 vary as the signal to noise ratio of the line emission measurement and the confidence level in the transition probability. The absolute line intensity, line intensity relative to the adjacent continuum, and the transition probability error are shown in Table 1a,b. The comparison

Table 1a. Spectral Emission Data for Air Arcs at 30 Atmospheres

Line	Relative I_{λ_o}	$I_{\lambda_{o_2}}/I_{\lambda_c}$	$\frac{dA_{ki}}{A_{ki}}$ +	E_{j_k} + (ev)	$E_{K_1}-E_{K_2}$ (ev)	$\frac{kT}{E_{j_k}}$ Δ	$\frac{kT}{E_{K_1}-E_{K_2}}$	$\left[\frac{d\epsilon_{\ell_j}}{\epsilon_{\ell_j}}+\frac{dA_{ki}}{A_{ki}}\right]\frac{kT}{E_{j_k}}$ ΔΔ	$\left[\frac{d(\epsilon_{\ell_1}/\epsilon_{\ell_2})}{\epsilon_{\ell_1}/\epsilon_{\ell_2}}+\frac{d(A_1/A_2)}{A_1/A_2}\right]\frac{kT}{E_{K_1}-E_{K_2}}$
NI 871.8	1.0	2.0	25 %	11.774	.007	.073	123.00	2.56 %	8,610 %
NI 871.1	1.5	3.0	25 %	11.770	.003	.073	287.00	2.56 %	20,090 %
NI 870.3	1.2	2.5	25 %	11.767	-*	.073	-*	2.56 %	-*
NI 865.5	.5	1.0	25 %	12.139	.372	.071	2.32	2.49 %	162 %
NI 862.9	4.5	9.0	25 %	12.144	.377	.071	2.29	2.49 %	160 %
NI 859.0	1.5	3.0	25 %	12.139	.372	.071	2.32	2.49 %	162 %
NI 856.7	.8	1.5	25 %	12.144	.377	.071	2.29	2.49 %	160 %
OI 844.6	29.0	29.0	10 %	11.004	-**	.073	-**	.73 %	-*
ArI 763.5	12.5	5.0	25 %	13.191	-*	.065	-*	2.28 %	-**
ArI 738.3	9.0	1.8	25 %	13.321	.130	.065	6.63	2.25 %	464 %
ArI 715.8	8.0	1.3	25 %	15.035	1.844	.057	.41	2.00 %	28 %
ArI 706.7	4.0	.8	25 %	13.321	.130	.065	6.63	2.25 %	464 %
ArI 696.5	5.0	.8	25 %	13.347	.156	.065	5.52	2.25 %	387 %

* Line used for E_{K_2}

** No lines available for E_{K_2}

Δ T is assumed to be 10,000°K

ΔΔ $\frac{d\epsilon_{\ell_j}}{\epsilon_{\ell_j}}$ is assumed to be 10%

\+ Energy levels and $\frac{dA_{ki}}{A_{ki}}$ taken from Reference [18]

Table 1b. Spectral Emission Data for Argon Arcs at 30 Atmospheres

Line	Relative I_{λ_o}	$I_{\lambda_{o_\ell}}/I_{\lambda_c}$	$\frac{d\lambda_{ki}}{A_{ki}}^{+}$	E_{j_k} (ev)$^{+}$	$E_{K_1}-E_{K_2}$ (ev)	$\frac{kT}{E_{j_k}}^{\Delta}$	$\frac{kT}{E_{K_1}-E_{K_2}}$	$\left[\frac{d\epsilon_{\ell_j}}{\epsilon_{\ell_j}}+\frac{d\lambda_{ki}}{A_{ki}}\right]^{\Delta\Delta}\frac{kT}{E_{j_k}}$	$\left[\frac{d(\epsilon_{\ell_1}/\epsilon_{\ell_2})}{\epsilon_{\ell_1}/\epsilon_{\ell_2}}+\frac{d(A_1/A_2)}{A_1/A_2}\right]\frac{kT}{E_{K_1}-E_{K_2}}$
ArI 826.4	2.0	20.0	25 %	13.347	.156	.065	5.523	2.28 %	386 %
ArI 794.8	10.0	50.0	25 %	13.302	.111	.065	7.762	2.28 %	543 %
ArI 763.5	29.0	97.0	25 %	13.191	-*	.065	-*	2.28 %	-*
ArI 738.3	20.5	41.0	25 %	13.321	.130	.065	6.628	2.28 %	464 %
ArI 727.2	3.5	7.0	25 %	13.347	.156	.065	5.523	2.28 %	387 %
ArI 715.8	1.5	3.0	40 %	15.035	1.844	.057	.467	2.85 %	37 %
ArI 706.7	16.4	27.3	25 %	13.321	.130	.065	6.628	2.28 %	464 %
ArI 696.5	18.4	30.7	25 %	13.347	.156	.065	5.528	2.28 %	387 %
ArI 430.0	1.0	.7	25 %	14.527	1.336	.059	.645	2.07 %	45 %

* Line used for E_{K_2}

$^{\Delta}$ T is assumed to be 10,000°K

$^{\Delta\Delta}$ $\frac{d\epsilon_{\ell_j}}{\epsilon_{\ell_j}}$ is assumed to be 10 %

$^{+}$ Energy levels and $\frac{dA_{ki}}{A_{ki}}$ taken from Reference [18]

of the error of the absolute line technique and line ratio technique from the air and argon spectra shows several lines available for diagnostics. However, the spectral absorption in the optical path must be determined for line candidates. The optical thinness [12] of the arc and optical path absorption must be measured before the temperature can be deduced from the emission spectra. Hence spectral and spatial absorption knowledge is necessary for line selection.

The air arc transmission of the HgI 546.4 line as seen in Figure 16 shows strong absorption which increases with air percentage. The slight loss of the 30 atm argon arc is relatively minor when compared to the air arc as seen in Figure 16. Also, refractive effects are noted in the transmission near the channel wall as seen by the signal loss region in the spatial transmission in Figure 15.

The relatively strong 546.4 line at an intermediate spectral position is strongly absorbed by small amounts of air and its byproducts. Moderate amounts of air as evidenced by the field strength of 34 V/cm and the large signal loss plus the lack of measurable signal at air purity (70 V/cm) indicate that a strongly absorbing medium is present in the air arc and its byproducts at a wavelength of 546.4 nm. The air to argon arc transition can be accomplished in less than 30 seconds as compared to the slow transmission recovery as seen when the arc is cycled from air to argon and the transmission shows little immediate response as evidenced by the

absorption of the argon emission as shown in Figure 17c. Thus, it is possible that the major absorption phenomena lies between the arc and the chamber in the narrow window plate area. The chamber area has not been contaminated, as seen by the clear view of the breather ports with no color change, during the experiment.

The spectral absorption at the arc center is measured over the 350.0 nm to 600.0 nm region by the mercury lamp transmission. The comparison of the spectra in Figures 17a,b from the chopped signal show a stronger absorption effect in the 350 nm to 400 nm region. However, the isolated mercury lines do not allow an identification of the absorbing medium. The comparison of the arc emission spectra as shown in Figure 17c shows that the argon arc emission is strongly absorbed by the air arc byproducts. The transmission spectrum shown in Figure 18b by Hall [20] is for the NO_2 molecule. A comparison of the emission spectra of Figure 17c and Figure 18b shows a one to one correspondence in the structure of the transmission in this experiment and the absorption spectra of Hall. Also, note the stronger absorption of the mercury lines in the 350 to 400 nm region and the peak in the absorption coefficient of NO_2 at 400 nm.

The spectral absorption characteristics of the arc byproducts are compared in Figure 19 immediately after arc extinction and at 50% recovery of the HgI 546.4 line. The

recovery of the transmission of the mercury lamp shows a spectral dependence on wavelength. The mercury lines from 350.0 nm to 450.0 nm show the strongest absorption effect. Hence, the spectral transmission must be determined on a local basis.

CHAPTER VII

CONCLUSIONS

The use of argon gas as a working medium for the pressurization of the chamber and protection of the electrodes is excellent at pressures up to 100 atmospheres. Argon gas at normal temperature and at pressures from 1 to 100 atmospheres shows negligible optical absorption at a wavelength of 546.4 nm. The cascade arc electrodes can be protected in an argon blanket while a reactive gas is contained in the central arc channel region. Slight apparatus shifts in the optical path during pressurization of the chamber assembly can be corrected by the use of optical beamshifters.

Argon arcs display a slight absorption effect in the central arc region with strong refractive effects at the arc wall. This results in a slight signal loss at the arc axis which extends as a plateau toward the arc channel wall. Strong refractive effects resulting in large signal losses are present at the channel wall due to the sharp thermal gradient and resulting density gradient.

Small amounts of air in a 30 atmosphere argon arc cause major transmission losses along the optical path at 546.4 nm. Strong refractive effects are also present in the wall region. Spectral absorption is present in the

300.0 nm to 900.0 nm wavelength region with the strongest effect located in the 350.0 nm to 500.0 nm band. The production of the NO_2 by the air arc is a major component of absorption in the outer boundary of the arc across the entire spectral range. The presence of other absorbing species were not determined because of the presence of strong NO_2 effects. No statement can be made on the effects of line and continuum absorption in the air plasma because of the predominance of the NO_2 band absorption outside the arc. The fast cycling of the arc from air to argon without the immediate recovery in the transmission suggests that the NO_2 and other byproducts are trapped in the narrow window plate gap of .010 in.. The large chamber area appears to be an excellent diffuser of the air arc byproducts since no absorption effects are visibly present in the outer breather ports which contain a pure argon arc.

Many lines are available for diagnostics for temperature measurements in the low pressure air and argon arcs. However, strong broadening effects and the increase in continuum emission with pressure results in the loss of available lines as the pressure is increased. The line ratio technique does not appear to be favorable due to the lack of lines with significantly differing energy levels. Since the second ionization stages are not evident, these lines have $KT/\varepsilon_1-\varepsilon_2 > 1$. The absolute line technique appears to be the most accurate method since KT/ε_{j_k} is usually $<<1$

for all the lines. The optical thinness of the lines must be verified so that the application of the Abel inversion can be validated. Optical thickness of more than 20% [19] results in error in the use of the Abel Inversion due to the loss of information within the arc.

CHAPTER VIII

RECOMMENDATIONS

The use of a wall-vortex stabilized cascade arc appears to be an excellent diagnostic tool for the investigation of the properties of air and argon arcs. The radiative, thermodynamic, and transport properties and their interactions are experimentally observable with potential for detailed diagnostics. The theoretical predictions for the plasma phenomena may be critically assessed to provide needed information for engineering applications.

The use of a stronger lamp source, such as a 1000 watt mercury or xenon lamp would aid in the diagnostics of any severe spectral absorption and refraction. Extension of spectral measurements to the infrared region may reduce the absorption effect on temperature determination techniques and provide additional lines for diagnostic applications.

The absorption and refraction effects must be separated to provide estimates of the true emission from the arc. The absorption within the arc and along the optical path must individually be assessed to determine the true radiative transport along the optical path. Also, the refractive effect at the wall must be separated from the refraction within the arc. A solid optical path to the boundary of the arc, a

stronger backlight source, and an extension of the spectral range of observation should provide for a precision measurement of the combined absorption and refraction effects.

The production of NO_2 by the air arc appears to be a neglected process in the prediction of the thermodynamic state. Although it may not be important in thermophysical calculations within the arc, the strong absorption effects even at low partial pressures make it an important component in the radiative transfer in the arc and heat transfer at the wall. The presence of strong diffusive effects, as evidenced by the NO_2 dispersion, requires the investigation of the L.T.E. equilibrium state composition in the presence of a thermal field.

The concentration of the air arc byproducts may be reduced by modifying the design of the cascade arc. The window plate gap could be increased to form a larger cross-sectional area for the diffusion of the arc byproducts. The complete removal of the window port cutout material in the test section area would reduce the length of the optical path from the arc to the chamber area. In addition, an increase in the distance from the air injection section and the window test section may allow for further thermal development of the arc channel resulting in a higher gas temperature at the channel wall and a reduction of the NO_2 mole fraction.

BIBLIOGRAPHY

1. W. E. Nicolet, et al., "Analytical and Design Study for a High-Pressure, High-Enthalpy Constricted Arc Heater," Aerotherm/Acurex, Mountain View, CA, available as report AEDC-TR-75-47 (AD-A012551), Arnold Engineering Development Center, July 1975.

2. S. D. Thompson, "Radial Temperature Profiles in an RF Plasma over a Wide Range of Applied Magnetic Field Intensities; Theory and Experiment," Ph.D. Thesis, Georgia Institute of Technology, Feb. 1974.

3. Larson, A. V. and Williams, J. R., "Electrical and Thermal Conductivity and Radiation Strength of Air Plasma at 1-30 Atm. and 6500-11,500°K," Final Report, Arnold Engineering Development Center, Contract F40600-74-0007, Arnold A.F. Station, Tenn.

4. R. S. Devoto, "Transport Coefficients of Ionized Argon," The Physics of Fluids, Vol. 16, No. 5, May 1973.

5. M. C. Wynn, "Investigation of Argon Plasma Properties at High Pressure," M.S. Thesis, School of Mechanical Engineering, Georgia Institute of Technology, 1975.

6. H. R. Griem, "High Density Corrections in Plasma Spectroscopy," Physical Review, Volume 128, No. 3, November 1, 1962.

7. H. R. Griem, "Validity of Local Thermal Equilibrium in Plasma Spectroscopy," Physical Review, Volume 131, No. 3, August 1, 1965.

8. I. A. Krinberg, "Composition and Properties of Air in a System with a Temperature Gradient," Teplofiz. Vys. Temp., 5, 5, pp. 936-938, Sept.-Oct. 1967.

9. V. A. Belov, and B. N. Sakontikov, "Composition Determination for a Mixture of Reacting Gases in a Cell with a Temperature Gradient," Teplofiz. Vys. Temp. 9, 2, pp. 436-438, March-April 1971.

10. A. I. Rozlovskii, "Formation of Nitric Oxide in the System N-N2-O-O2," Kinetika i Kataliz, 8, 6, pp. 212-1216, Nov.-Dec. 1967.

11. M. T. Dmitriev and Yu A. Sorokin, "Radiation Chemical Formation of Nitrogen Oxide in the System Nitrogen-Oxygen at Elevated Temperatures," Zhurnal Rrik. Khimii, 37, 4, pp. 727-734, April 1964.

12. H. R. Griem, Plasma Spectroscopy, McGraw-Hill, N. Y., 1964.

13. V. Oklobdzya and N. Konjevic, "Refractive-Ray Bending in Axially Symmetric Plasma Sources," J. Quant. Spectrosc. Radiat. Transfer, 14, pp. 389-394, 1974.

14. A. I. Kharitonov. K. S. Khoroshko, and V. P. Shkadova, "Temperature Dependence on Air Refraction at High Temperatures," Izvestiya Akademii Nauk SSSR, Mekhanika Zhidkosti i Gaza, 5, pp. 177-180, Sept.-Oct. 1974.

15. R. H. Huddlestone and S. L. Leonard, "Plasma Diagnostic Techniques," Academic Press, N. Y., 1965.

16. A. S. Predvoditelev, et al., Tables of Thermodynamic Functions of Air for the Temperature Range 6,000-12,000°K and Pressure Range 0.001-1000 Atm., Infosearch Limited, London, distributed by Cleaver-Hume Press Ltd.

17. H. W. Drawin and P. Felenbok, Data for Plasmas in Local Thermodynamic Equilibrium, Gauthier-Villars, Paris, 1965.

18. National Standards Reference Data Series, National Bureau of Standards, No. 22, Vol. 2.

19. G. S. Ambrok, "Radial Radiation Intensity Distribution in a Dense Axisymmetric Plasma," Zh. Rrik. Spekt. 14, 3, pp. 383-388, March 1971.

20. T. C. Hall, Jr. and F. E. Blacet, "Absorption Spectra of NO_2," J. of Chem. Phys. 20, 1745, 1952.

21. E. A. Ershov-Ravlow, L. S. Kiselevskii, N. I. Chubrik, and V. D. Shimanovich, "Absorption of Air Plasma in the Near IR Spectral Region," Zh. Rrik. Spekt. 19, 6, pp. 995-1000, Dec. 1973.

22. V. A. Gubkevich, E. A. Ershov-Pavlov, L. I. Kiselevskii, N. S. Chubrik, and V. D. Shimanovich, "Experimental Investigation of the Radiative Properties on an Air Plasma in the Spectral Range 400-1200 n., Zh. Prik. Spekt. 24, 2, pp. 219-226, February 1976.

23. F. R. Gilmore, "The Contribution of Generally-Neglected Band Systems to the Absorption Coefficient of High Temperature Air," J.Q.R.S.T., 5, pp. 125-135.